This is a non-peer reviewed EarthArXiv preprint version that has been submitted for publication in IEEE Transactions on Geoscience and Remote Sensing.

# Tracking Progress in General-Purpose VLMs and Agents for Earth Observation

Skyler D. Liu, Sherrie Wang

***Abstract*—The rapid advancement of vision-language models (VLMs) and agent-based workflows is expanding their potential for Earth observation (EO). Existing studies primarily compare models at a single point in time, providing limited insight into how their capabilities evolve across generations. To address this gap, we conduct a longitudinal evaluation of 48 VLMs across successive generations using a benchmark comprising 13 EO tasks, examining both overall EO performance and individual task capabilities. We investigate the effects of prompting strategies, task-specific fine-tuning, agent-based inference, and reasoning effort, as well as its association with model parameter count. Results reveal substantial but uneven progress in the EO capabilities of general-purpose VLMs. Object classification, scene understanding, and object counting improve markedly, while change detection and precise localization also improve but remain challenging. Few-shot prompting and task-specific fine-tuning provide performance gains, whereas chain-of-thought and increased reasoning effort sometimes degrade model performance. Holding the underlying model fixed, autonomous agent-based inference significantly improves GPT-6 Astra's overall EO score ($+4.59$ points; $p = 0.025$), with the largest gains in object counting and change detection. These findings demonstrate that model evolution and improved execution workflows are advancing the EO capabilities of general-purpose VLMs, while fine-grained visual perception and spatial reasoning remain major challenges.**

***Index Terms*—AI agents, Earth observation, longitudinal evaluation, vision-language models.**

## I. Introduction

EARTH observation (EO) provides valuable insights into sudden disasters and long-term changes across the Earth's surface. It helps assess damage to buildings and farmland, monitor wildlife populations and forest ecosystems, track changes in water resources, and support transportation infrastructure management. Its practical value lies in extracting actionable information from imagery, such as what objects are present, how many there are, how they have changed, and where they are located. Producing such information typically requires task-specific models, annotated training data, and expertise in remote-sensing analysis [1], [2]. However, general-purpose vision-language models (VLMs) may be able to address diverse EO tasks using a single model guided by natural-language instructions, reducing the need to develop separate pipelines for individual applications.

Compared with conventional natural-image understanding tasks, EO requires not only scene-level understanding but also fine-grained perception of individual objects and their spatial relationships. In overhead imagery, objects vary considerably in scale, may occupy only a few pixels, and often appear against complex backgrounds, making instance-level perception and precise spatial reasoning particularly challenging [1], [3]–[7]. Early work by Zhang and Wang found that general-purpose VLMs perform relatively well in scene understanding but struggle with object counting, change detection, and precise localization [2]. Subsequent studies have further confirmed the gap between semantic understanding and quantitative or spatial accuracy [8]–[10]. However, as models within the same family continue to evolve, it remains unclear whether these strengths persist, existing weaknesses improve, or certain capabilities regress.

Existing studies primarily compare model performance at a single point in time. However, as new generations of models are released, such evaluations can quickly become outdated and provide limited insight into the long-term evolution of model capabilities. A single evaluation is particularly insufficient to distinguish sustained progress, stagnation, and performance fluctuations across different tasks. Therefore, longitudinal evaluation across model generations under a unified evaluation framework is essential for systematically tracking overall and task-specific performance, revealing the progress and persistent limitations of general-purpose VLMs from a broader, long-term historical perspective, and informing model selection and future EO research.

Model evolution is not the only route to improving EO performance. Beyond adopting stronger base models, performance can also be improved through few-shot prompting, chain-of-thought (CoT) reasoning, fine-tuning, and agent-based workflows. These approaches aim to improve model performance in different ways: few-shot prompting uses examples to help models understand task requirements; CoT encourages step-by-step reasoning; task-specific fine-tuning adjusts model parameters to better adapt to specific tasks; and agents enhance the model's ability to handle complex tasks through autonomous planning and tool use, decomposing tasks into multiple steps and integrating local image analysis, code execution, self-verification, and result aggregation. Beyond advances in the underlying models, improvements in inference and model-use strategies may further enhance their EO capabilities. Therefore, it is important to systematically evaluate whether these strategies provide additional performance gains

Skyler D. Liu is with the Massachusetts Institute of Technology, 77 Massachusetts Avenue, Cambridge, MA 02139-4307, USA (e-mail: liudong@mit.edu). Sherrie Wang is with the Department of Mechanical Engineering, Massachusetts Institute of Technology, 77 Massachusetts Avenue, Cambridge, MA 02139-4307, USA (e-mail: sherwang@mit.edu). (*Corresponding author: Sherrie Wang.*)

This article has supplementary material provided by the authors.

This work has been submitted to the IEEE for possible publication. Copyright may be transferred without notice, after which this version may no longer be accessible.

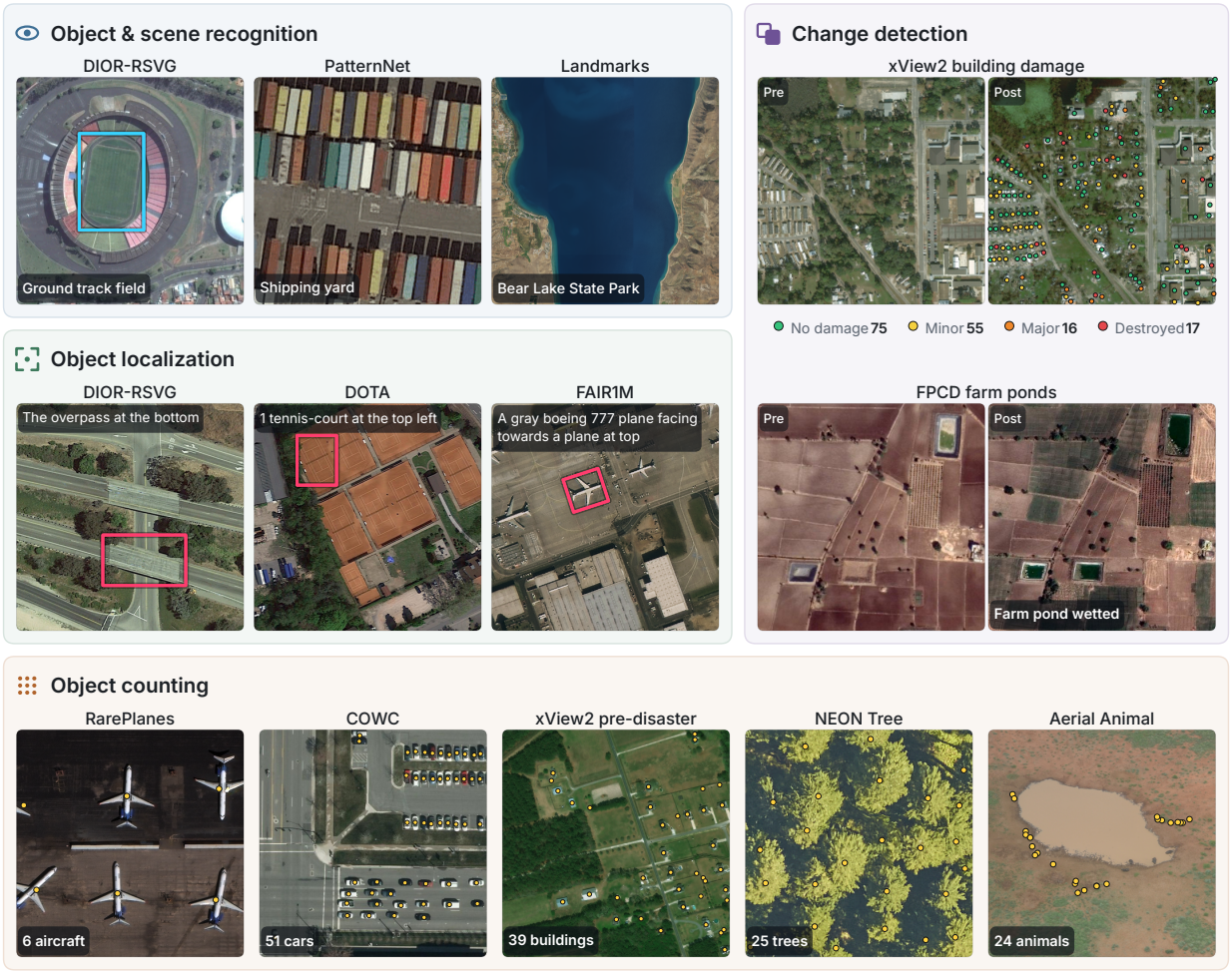



Fig. 1. Overview of the 13 EO tasks used to evaluate VLM capabilities, spanning object and scene recognition (object categories, scene types, and landmarks), object counting (aircraft, cars, buildings, trees, and animals), change detection (building damage and farm pond changes), and object localization (locating targets in remote sensing images based on natural-language descriptions). Representative examples show the corresponding ground-truth annotations.

while tracking progress across model generations. Examining model evolution and model-use strategies together can provide a more comprehensive understanding of the progress of general-purpose VLMs in EO and their potential for further improvement.

To this end, we conduct a longitudinal evaluation of 48 models from four major proprietary and open-source model families from 2023 to 2026: GPT, Gemini, Qwen, and LLaVA. Our unified benchmark comprises 13 tasks and 7,273 test samples (Fig. 1), organized by the spatial granularity of their required outputs: coarse-grained object and scene recognition, medium-grained object counting, and fine-grained change detection and localization. Using consistent task definitions and evaluation procedures, we track zero-shot performance by public release date and examine its relationships with model parameter scale and reasoning effort. Complementary experiments further investigate the effects of few-shot prompting, CoT reasoning, and task-specific fine-tuning on model performance. We also introduce an agent-based workflow using the OpenAI Agents API while holding the underlying model fixed, allowing us to isolate the additional gains from agent-based inference. Furthermore, we use specialized EO models as task-specific reference points to identify where general-purpose VLMs are approaching specialized performance and where dedicated methods remain necessary.

Our results reveal substantial but uneven progress in the EO capabilities of general-purpose VLMs. From a longitudinal perspective, later model releases generally achieve higher overall performance, although different model families and tasks exhibit distinct trajectories, with progress in some capabilities remaining non-monotonic. Model performance is closely related to the spatial granularity required by the task. VLMs perform strongly on coarse-grained tasks such as object classification and scene recognition, while performance on medium-grained object counting depends on target characteristics and scene complexity. Fine-grained tasks, including change detection and precise localization, remain particularly challenging. Further experiments show that few-shot prompting and task-specific fine-tuning provide relatively consistent performance gains, whereas CoT reasoning and increased reasoning effort can sometimes degrade performance due to excessive reasoning. Moreover, holding the underlying model fixed, autonomous agent-based inference significantly improves GPT-6 Astra's overall EO score by 4.59 points

($p = 0.025$). In contrast, predefined task-specific human guidance provides virtually no additional improvement in overall performance. Overall, these findings reveal both the progress and persistent limitations of general-purpose VLMs in EO, demonstrating that model performance depends not only on the evolution of the underlying models but also on task characteristics, inference strategies, and execution workflows.

The main contributions of this work are fourfold:

- **Longitudinal evaluation across model generations.** We conduct a longitudinal evaluation of 48 general-purpose VLMs across 13 EO tasks and, under a unified evaluation protocol, analyze how the overall and task-specific performance of major proprietary and open-source model families evolves over time.
- **Effects of inference strategies and reasoning effort.** We systematically evaluate the effects of different inference and adaptation strategies, including few-shot prompting, CoT reasoning, and task-specific fine-tuning, as well as varying levels of reasoning effort, on EO performance. We further characterize how the benefits of these approaches differ across task types.
- **Agent-based workflows.** Motivated by the growing use of agent-based workflows, we evaluate agent performance on EO tasks using the OpenAI Agents API. Through a comparison of the standard API with autonomous and human-guided agent workflows, we show that agent-based workflows can further improve the EO task performance of the underlying model, particularly in object counting and change detection.
- **Capability boundaries and comparison with specialized EO models.** We analyze the relationships between model performance, task spatial granularity, and target characteristics, using specialized EO models as reference points to identify which tasks are increasingly within the reach of general-purpose VLMs and which capabilities still require dedicated methods and further research.

## II. Related Work

### A. Evaluation of General-Purpose VLMs for EO

As general-purpose vision-language models (VLMs) have demonstrated strong capabilities in natural-image understanding, researchers have increasingly investigated whether these capabilities transfer to remote sensing and Earth observation (EO). Zhang and Wang conducted an early systematic evaluation of general-purpose VLMs on EO tasks through VLEO-Bench, covering scene understanding, object localization and counting, and change detection. Their findings showed that GPT-4V performed relatively well in scene-level semantic understanding and open-ended image captioning, but struggled with object counting, precise localization, and disaster change analysis, which require fine-grained spatial understanding [2]. Subsequently, VRSBench extended VLM evaluation to richer semantic and instance-level remote-sensing tasks through image captioning, visual grounding, and visual question answering [8]. MME-RealWorld incorporated remote-sensing scenarios into a general high-resolution multimodal large language model (MLLM) benchmark and evaluated models including GPT-4o, Gemini, and Claude, further highlighting the challenges of small-object perception and complex spatial understanding [4].

Other studies have further expanded the scope of remote-sensing VLM evaluation. GEOBench-VLM introduced 31 fine-grained tasks covering scene understanding, object classification and counting, localization, segmentation, temporal analysis, and non-optical data understanding, evaluating both general-purpose VLMs and specialized remote-sensing models [9]. CHOICE developed a hierarchical evaluation framework for perception and reasoning, comprising 23 tasks and 10,507 questions, and compared three proprietary and 21 open-source models [10]. XLRS-Bench and LRS-VQA focused on understanding ultra-high-resolution remote-sensing imagery. The former evaluated 16 categories of perception and reasoning tasks, while the latter used images with side lengths of up to 27,328 pixels to assess the ability of models to understand large-scale scenes and localized targets [5], [6]. RSVLM-QA further evaluated mainstream general-purpose VLMs on remote-sensing visual question answering tasks, focusing on semantic understanding, spatial relationship reasoning, and object counting [7].

Despite the growing coverage of tasks and models, existing benchmarks primarily rely on cross-sectional evaluations, comparing models available at a particular point in time. As foundation models evolve rapidly, such evaluations can quickly become outdated and provide limited insight into whether previously identified strengths persist, whether known limitations have been overcome, and how capabilities across different tasks evolve over model generations. In contrast, our study conducts a longitudinal evaluation of successive releases from multiple major model families under a unified evaluation framework. By tracking changes in overall performance and systematically examining task-specific progress, we reveal the advances, persistent limitations, and evolving capability boundaries of general-purpose VLMs in EO from a broader, long-term historical perspective, thereby informing model selection and future EO research.

### B. Evaluation of Agent-Based Workflows for EO

Beyond the evaluation of general-purpose VLMs, recent research has also begun to develop benchmarks for systematically assessing the capabilities and limitations of agents in remote sensing and EO tasks. Wang et al. introduced DORA, a benchmark for disaster-response agents comprising 515 tasks from 45 real-world disaster events and 108 specialized geospatial tools. It evaluates agents across disaster perception, spatial analysis, operational planning, temporal reasoning, and report generation. The results reveal persistent challenges in tool selection, argument grounding, and error accumulation during multistep execution [11]. This study highlights the challenges of reliable agent execution and suggests that additional execution steps do not necessarily lead to better results.

Existing benchmarks for agents in EO have primarily focused on the specific application scenario of disaster response, and typically rely on specialized remote-sensing or geospatial tools. In contrast, our study evaluates whether fully managed,

general-purpose agent workflows can improve VLM performance across diverse EO tasks without relying on specialized toolchains, and how their benefits vary across task categories. Furthermore, we examine whether predefined task-specific human guidance can further improve performance compared with fully autonomous agents.

## III. Benchmark and Evaluation Protocol

### A. Task Suite and Datasets

To systematically evaluate how VLM capabilities evolve across model generations, we build on the RGB-based tasks in two EO benchmarks, VLEO-Bench [2] and GEOBench-VLM [9]. While these studies evaluate models at a single point in time, we extend the evaluation across successive model generations to track their progress. We evaluate 48 VLMs across 13 EO tasks and 7,273 test samples, covering coarse-, medium-, and fine-grained EO capabilities (Fig. 1).

Coarse-grained tasks comprise two categories: object classification and scene recognition. Object classification uses DIOR-RSVG to evaluate the ability to identify object categories, while scene recognition uses PatternNet [12] and Landmarks Recognition to assess the recognition of scene types and landmarks. Medium-grained tasks are counting problems for RarePlanes Aircraft [13], COWC Car [14], xView2 Pre-disaster Building [15], NEON Tree [16], and Aerial Animal [17]. Fine-grained tasks include xView2 Change Detection [15], FPCD Farm Pond Change Detection [18], and DIOR-RSVG, DOTA [19], and FAIR1M [20] localization, which test temporal change understanding and spatial localization.

We exclude some tasks from the original benchmarks for data quality and sample availability reasons. For example, RSICD Image Captioning is excluded because multiple descriptions of the same image can be correct, making it difficult to evaluate generated captions reliably. We exclude fMoW-WILDS [21], [22] because some categories overlap or have unclear boundaries, making classification results harder to interpret. PatternNet already provides a representative scene recognition task. Water-body Counting is excluded because of its relatively small sample size.

### B. Model Selection and Release Timeline

We select four mainstream, representative model families spanning closed-source and open-source models: GPT, Gemini, Qwen, and LLaVA. We did not include Claude because many of the high-resolution remote-sensing images used in our evaluation exceed its per-query image-input token limit, resulting in API errors. To characterize long-term progress, we evaluate 48 models across these four families, spanning releases from 2023 to 2026, and organize their results chronologically by public release date, as illustrated in Fig. 2.

### C. Evaluation Settings

*1) Zero-Shot Evaluation:* All 48 models in the longitudinal analysis are evaluated in a zero-shot setting, without in-context demonstrations. Each model is evaluated using its default reasoning-effort setting, without manually adjusting the reasoning effort. To ensure comparability across models and release generations, we use the same task definitions, task-specific prompts, and output requirements for each task. Responses are converted into labels, counts, or bounding boxes using task-specific parsing rules before metric computation. The complete system messages and user prompt templates for all tasks are provided in Section S.1 of the Supplementary Material. This standardized evaluation protocol allows us to track performance changes across the 13 EO tasks and analyze how model capabilities evolve across generations.

*2) Chain-of-Thought, Few-Shot, and Fine-Tuning:* Beyond zero-shot evaluation, we investigate the effects of Chain-of-Thought (CoT) reasoning [23], four-shot prompting, and task-specific fine-tuning on EO task performance. Specifically, CoT prompting instructs the model to provide image-based reasoning before its final answer. Four-shot prompting adds four image-question-answer demonstrations before the test query, selected from the corresponding dataset's training partition, excluding test images. Further details and examples are provided in Section S.2 and Fig. S1 of the Supplementary Material.

For task-specific fine-tuning, we select Qwen3-VL-32B and LLaVA-OneVision-2-8B from the Qwen and LLaVA open-source model families, respectively, and fine-tune both models using Quantized Low-Rank Adaptation (QLoRA) [24], which builds on Low-Rank Adaptation (LoRA) [25]. The fine-tuning configurations and computational resources are detailed in Section S.3 of the Supplementary Material.

*3) Model Scale Analysis:* To examine the relationship between model scale and EO capability, we analyze 23 Qwen and LLaVA models with publicly reported parameter counts, relating log-parameter count to overall task performance. Closed-source models such as GPT and Gemini are excluded because comparable parameter-count information is not publicly available.

*4) Reasoning Effort:* To evaluate the effect of reasoning effort on EO performance, we select GPT-6.1 Sol and Gemini 3.8 Flash, two recent models from the GPT and Gemini families, respectively, at the time of manuscript submission. For each model, we keep the underlying model and evaluation protocol fixed while varying the available reasoning-effort settings, rather than using the default setting as in the zero-shot evaluation.

We record overall EO performance, mean thinking-token consumption, API response time, and API cost per 1,000 requests (USD) at each reasoning-effort level. Since response time is measured through API calls, it can be affected by network conditions and provider server load. To improve the comparability of API response times across reasoning-effort levels, we conducted the experiments in an interleaved manner over the same period.

*5) Agent-Based Workflows:* We further investigate whether agent-based inference can improve EO performance using OpenAI's Agents API [26]. The API provides a managed Codex harness that coordinates agent execution, maintains session state, and handles context compaction and recovery. We use an OpenAI-hosted sandbox, where the agent can

execute code and work with files. To reduce the risk of the agent retrieving dataset annotations or reference answers from the internet, we disable the web-search capability of the Agents API and explicitly instruct the agent not to perform web searches in the prompt.

We select GPT-6 Astra, one of the strongest representative models in our zero-shot evaluation, for the agent experiment and use the same underlying model for both the standard API and Agents API conditions. The agent condition provides an execution environment in which the model can autonomously plan its steps, use code and tools, perform self-verification, and iteratively reflect on its intermediate reasoning while working toward a final answer. Thus, this comparison evaluates the performance of the same model under two different workflows.

To keep agent-based inference costs low, we use stratified random sampling to select 100 test samples per task, or all available test samples for tasks with fewer than 100. Specifically, we group samples based on task-specific ground-truth annotations, such as class labels for classification and object counts for counting. We then randomly sample from each group in proportion to its size to preserve the original data distribution. We then evaluate the standard API and Agents API using the same underlying model and exactly the same test samples. This paired comparison avoids differences in test samples affecting the results, allowing us to more directly assess the performance gains from the agent-based workflow.

We conduct a comparative experiment using two Agents API workflows: Autonomous Agents API and Human-guided Agents API. The autonomous workflow uses the same task prompts as in the zero-shot evaluation, with only an additional instruction prohibiting web searches, allowing the agent to plan and execute tasks independently. The human-guided workflow additionally includes predefined, task-specific guidance describing how a human would approach each task. For example, in object localization, the prompt is "First break down the description into attributes, position, and relations. List all candidate targets. Eliminate candidates one by one using their position and relations. Zoom in on the target edges to tighten the box boundaries. Confirm that the coordinates are expressed in original-image pixels. Do not search the web for these datasets or data." The prompt protocol and task-specific guidance for both workflows are provided in Section S.4 of the Supplementary Material.

*6) Comparison With Specialized EO Models:* We compare zero-shot GPT-6 Astra with one specialized EO model for each of the 13 tasks, as summarized in Table I. We evaluate released specialized-model checkpoints on the same test samples as Astra. To avoid training–test overlap, we use held-out test subsets from PatternNet, DIOR-RSVG, DOTA, and FAIR1M, respectively. The remaining datasets do not present training–test overlap issues.

Unlike GPT-6 Astra, which is evaluated zero-shot without task-specific fine-tuning, all specialized EO models were trained on the training sets of their respective evaluation datasets, with one exception: EarthDial in the FPCD evaluation. Since no EarthDial checkpoint trained on FPCD is publicly available, we instead use a checkpoint trained on related change-detection datasets, such as LEVIR-MCI and xBD.

### D. Evaluation Metrics

Each task is evaluated using a primary metric suited to its output type. Scene understanding, object recognition, and FPCD change detection tasks use accuracy; localization tasks use mean Intersection over Union (mIoU); counting tasks use the squared Pearson correlation ($r^2$) between predicted and ground-truth counts. For xView2 Change Detection, we compute $r^2$ separately for each of the four damage categories (no damage, minor damage, major damage, and destroyed) using the predicted and ground-truth building counts, and report their equally weighted average (macro-averaged $r^2$).

For counting-based tasks, we primarily use $r^2$ because, unlike MAE and RMSE, it is naturally bounded between 0 and 1, with higher values generally indicating stronger correlation, making it easier and more natural to integrate with accuracy and mIoU into a unified overall score. More importantly, it reflects how well model predictions capture variations in object counts across images, potentially allowing systematic biases to be corrected through subsequent calibration even when counting errors are large [2]. In addition to $r^2$, we also report evaluation results using MAE and RMSE for object counting and xView2 Change Detection in Section S.10 of the Supplementary Material.

To compute the overall score, we first constrain each task's primary metric to the interval $[0, 1]$. Following a task-level aggregation approach similar to that used in the BRIDGE benchmark [27], we calculate the score for model $m$ as the equally weighted average across all its benchmark tasks:

$$S(m) = 100 \times \frac{1}{|T_m|} \sum_{t \in T_m} s(m, t), \tag{1}$$

where $T_m$ denotes all benchmark tasks for model $m$, and $s(m, t)$ is the normalized score of model $m$ on task $t$. Equal task weighting ensures that each task contributes equally to the overall score, regardless of its sample size. By aggregating accuracy, $r^2$, and mIoU across tasks, the overall score aims to summarize model performance across different EO tasks.

To assess the robustness of the overall scoring results, we consider two alternative evaluation approaches in Section S.10 of the Supplementary Material: category-balanced weighting and error-based counting metrics. We also conduct a leave-one-task-out analysis to assess sensitivity to individual tasks. The results show highly consistent model rankings (Spearman's $\rho = 0.96$–$1.00$), while the overall trend of performance improvement across model generations remains unchanged.

## IV. Progress Across Model Generations

We systematically examine how the EO capabilities of general-purpose VLMs evolve across model generations. We begin by analyzing overall performance trends over time, then investigate how progress differs across five task categories: object classification, scene understanding, object counting, change detection, and object localization. This analysis helps identify which capabilities have improved consistently and which remain challenging. Building on these findings, we

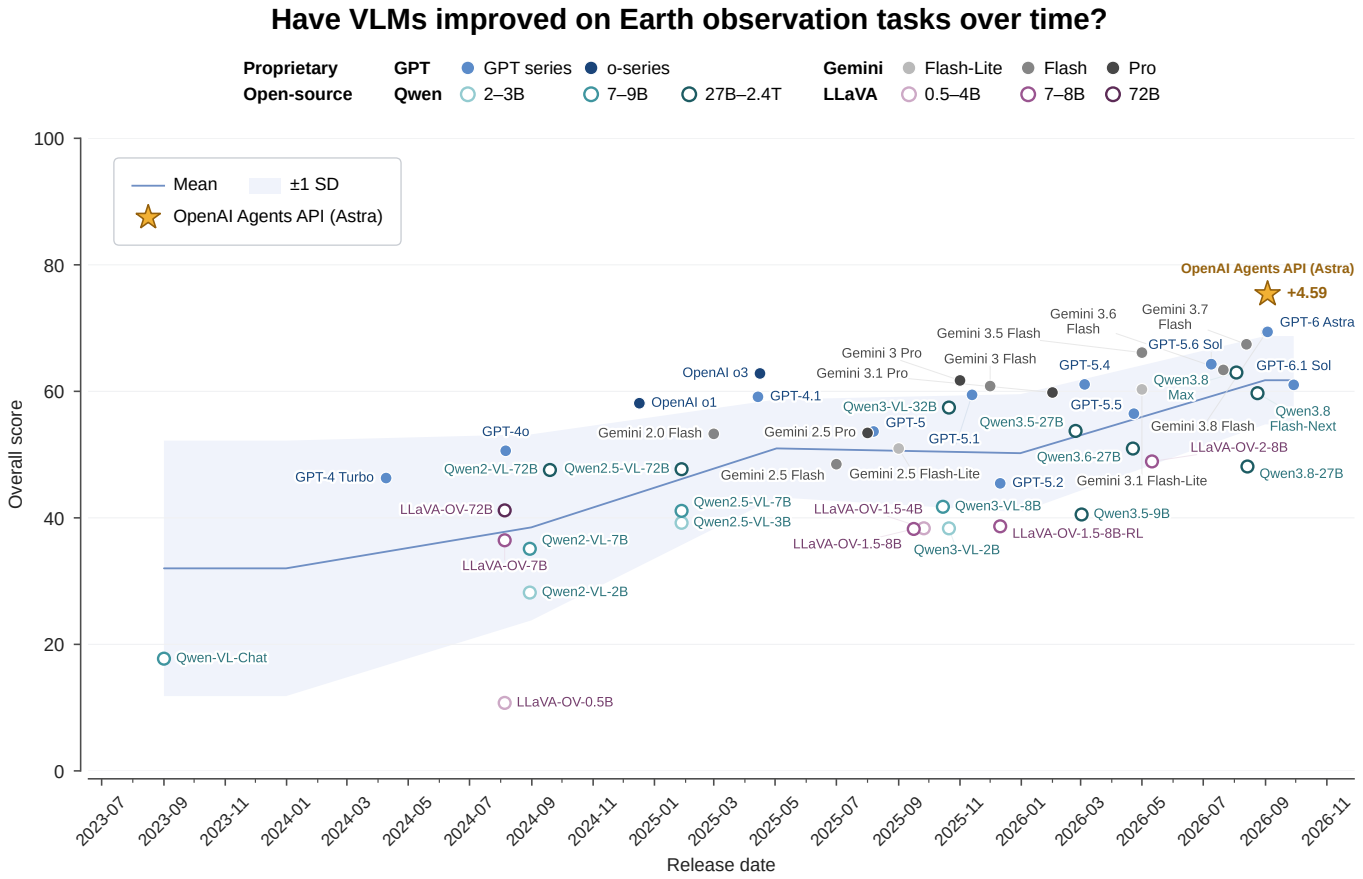



Fig. 2. Zero-shot overall EO performance generally shifts upward across successive VLM releases. Later models increasingly occupy higher-score regions, although progress between individual releases is not strictly monotonic. Agent-based inference further improves the overall performance of GPT-6 Astra while holding the underlying model fixed. Due to Agents API inference costs, the agent point uses stratified subsets of approximately 100 samples per task, while other points use full test sets. The labeled gain over Astra is computed on the same paired subsets.

further examine the capability boundaries of recent models and the relationships between model performance, parameter scale, and reasoning effort.

### A. *Overall Base Model Progress Over Time*

Fig. 2 presents the zero-shot overall EO scores of the evaluated models ordered by public release date. A clear upward shift is visible over time: the overall EO capability of general-purpose VLMs has improved substantially across model generations. The overall scores of individual models and their 95% bootstrap confidence intervals are given in Fig. S9 of the Supplementary Material.

This trend is not driven by a single model family. Both proprietary and open-source families include stronger models among their more recent releases, suggesting that the improvement reflects broader advances in general-purpose vision-language modeling rather than progress confined to a particular family. At the same time, the trajectory is not strictly monotonic: newer releases do not always outperform earlier ones, and temporary regressions or plateaus occur across model families. Overall, despite fluctuations between individual releases, the EO capabilities of general-purpose VLMs show a clear and sustained improvement over time.

The timeline also shows that advances in underlying model capabilities can be further enhanced through workflow improvements. For GPT-6 Astra, the agent workflow using the OpenAI Agents API achieves a higher overall score than direct model inference through the standard API, while keeping the underlying model fixed. We examine these workflow-level gains separately in Section V-B.

### B. *Task-Specific Progress Across Model Generations*

The improvement in overall performance does not imply that all EO capabilities progress at the same rate. Fig. 3 decomposes the longitudinal trend into object classification, scene understanding, object counting, change detection, and object localization, revealing distinct trajectories across both tasks and model families.

Object classification shows an overall upward trend, although performance fluctuates across individual releases (Fig. 3(a)). Recent GPT and Gemini models approach 100% accuracy, while newer Qwen models also improve markedly. Progress is less consistent for LLaVA, indicating that gains are not uniform across model families.

Scene understanding is one of the EO tasks on which current VLMs perform relatively well. As shown in Fig. 3(b),

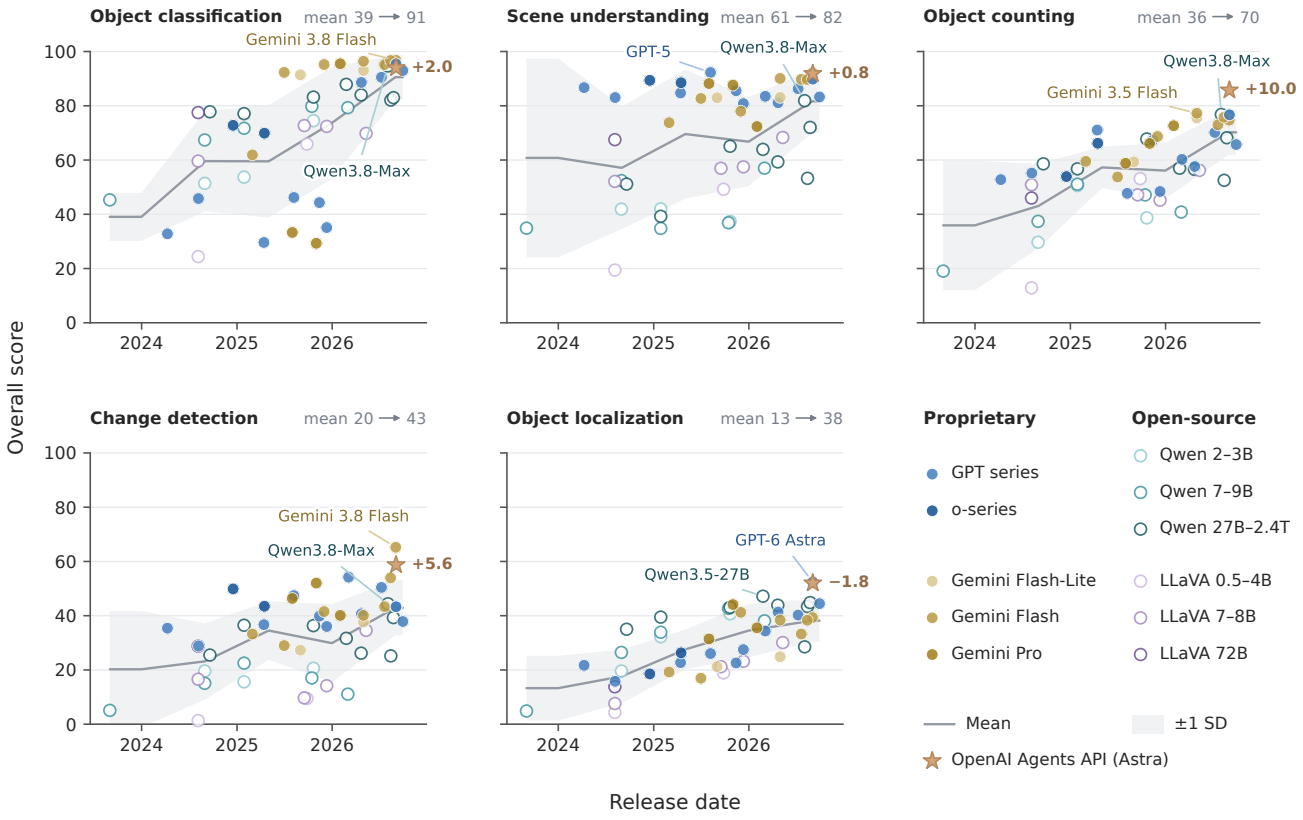



Fig. 3. VLMs show substantial but uneven progress in EO capabilities across successive model releases. Coarse-grained object classification and scene understanding improve markedly, medium-grained object counting also advances, while fine-grained change detection and localization improve as well but remain challenging. Agent-based inference provides further gains in counting and change detection, but not across all tasks. Due to Agents API inference costs, the agent point uses stratified subsets of approximately 100 samples per task, while other points use full test sets. The labeled gain over Astra is computed on the same paired subsets.

scene-understanding performance also generally improves over time. Proprietary models achieve relatively strong performance even in earlier releases and maintain this high level across subsequent generations. Open-source models begin from lower baselines but improve substantially with model evolution, with several recent releases markedly narrowing the gap with proprietary models.

Object counting shows particularly clear generational progress (Fig. 3(c)). Later releases generally outperform earlier models, indicating substantial improvements in object counting capabilities. This upward trend is observed within each model family, across both proprietary and open-source models. However, counting performance has not yet reached saturation. As shown in the following subsection, Current Capability Boundaries, substantial room for improvement remains for targets with complex signal structures; counting performance also varies considerably with target and scene structure, indicating that it remains highly sensitive to the visual characteristics of both the targets and their surrounding scenes.

Change detection also improves over time (Fig. 3(d)). Scores remain relatively low, indicating that jointly identifying and quantifying temporal changes between images remains challenging for general-purpose VLMs.

Object localization performance shows an overall upward trend across model generations (Fig. 3(e)). This trend is observed across all four model families, although performance fluctuates to varying degrees between releases.

Overall, VLMs show improvements across all five EO task categories, although the magnitude of improvement varies. As shown in Fig. 3, the mean score increases from 39 to 91 for object classification, from 61 to 82 for scene understanding, from 36 to 70 for object counting, from 20 to 43 for change detection, and from 13 to 38 for object localization.

As an exploratory exercise, we linearly extrapolate the historical trends of the five EO task categories to estimate when their mean scores might reach 90 (Section S.9, Fig. S4, and Table S4 of the Supplementary Material). As of 2026, object classification has already reached this level, with the latest mean score of 90.5. Based on the fitted trends, scene understanding is projected to reach 90 in 2028. Object counting is projected to reach 90 in 2029, whereas change detection and object localization are projected to reach 90 in 2034 and 2031, respectively. Notably, these results are based on linear extrapolation of historical trends and should not be interpreted

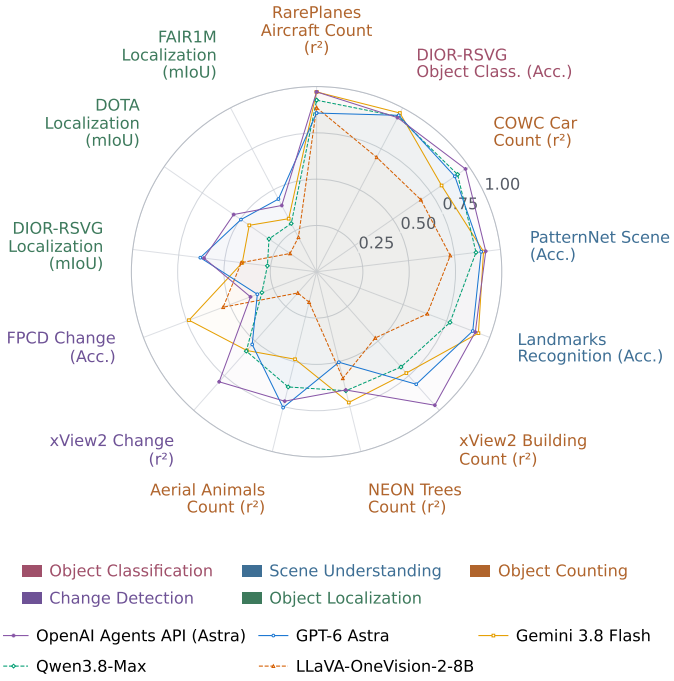



Fig. 4. Current VLMs exhibit uneven EO capabilities across task granularity levels. They perform well on coarse-grained object classification and scene understanding, while medium-grained object counting shows substantial performance variability depending on the visual signal structure of targets and backgrounds. Fine-grained change detection and object localization remain challenging. Agent-based inference improves some counting and change-detection tasks but does not fully overcome these limitations.

as reliable forecasts of future model performance.

### C. Current Capability Boundaries

To characterize the capability boundaries of current general-purpose VLMs, Fig. 4 summarizes the zero-shot performance of four representative models, one from each major model family. GPT-6 Astra (69.40) and Gemini 3.8 Flash (69.38) achieve nearly identical overall zero-shot scores, with Astra scoring only marginally higher. Qwen3.8-Max (63.0) and LLaVA-OneVision-2-8B (48.9) rank lower. However, no single model dominates across all EO capabilities.

From a task-level perspective, as tasks require increasingly fine-grained spatial understanding, a clear decline in capability emerges from coarse- to fine-grained tasks (Fig. 4).

Coarse-grained object recognition and scene understanding are the strongest capabilities of current models: the four-model mean scores are 0.892, 0.849, and 0.811 for DIOR-RSVG Object Classification, PatternNet Scene Recognition, and Landmarks Recognition, respectively. These tasks rely primarily on category-level semantics and holistic scene appearance, where the broad semantic knowledge acquired through large-scale pretraining provides an advantage for global image understanding.

Medium-grained counting performance depends on the image signal structure jointly determined by targets and backgrounds. When targets have regular shapes, moderate spatial density, and relatively simple backgrounds, models can more readily identify and count individual instances. For example, RarePlanes Aircraft Counting and COWC Car Counting achieve mean $r^2$ values of 0.910 and 0.834, respectively, across the latest models from the four families. In contrast, counting becomes substantially more difficult when targets have more irregular shapes, are very sparsely distributed, or are embedded in more complex backgrounds. The corresponding mean $r^2$ values are 0.677, 0.621, and 0.513 for xView2 Pre-disaster Building Counting, NEON Tree Counting, and Aerial Animal Counting, respectively. These results show that counting performance is strongly shaped by target-background signal structure, with target geometry, spatial distribution, and background complexity all substantially affecting the counting capability of VLMs.

Fine-grained change detection remains a major challenge for current VLMs. The four-model mean scores are 0.454 for xView2 Change Detection and 0.484 for FPCD Farm Pond Change Detection. For xView2, models must not only identify damaged buildings but also accurately classify their damage severity. From an overhead view, minor and major damage may both appear as partial roof damage, making it difficult to determine how severely a building is affected. Moreover, misclassifying a building's damage level affects the counts of the corresponding damage categories.

FPCD presents a different challenge: the changes themselves can be difficult to notice. Farm ponds are often small, and two images may look nearly identical even when the water extent has changed slightly. Changes in the surrounding farmland can further make it difficult to distinguish actual pond changes from background variations.

Precise object localization is similarly challenging. The four-model mean scores are 0.428 for DIOR-RSVG, 0.356 for DOTA, and 0.318 for FAIR1M. For example, a model may correctly recognize an aircraft but still fail to produce an accurate bounding box around it. Particularly for small objects, even a slight displacement of the predicted box can substantially reduce IoU. This indicates that even when a model correctly recognizes an object, it may not accurately localize it.

Overall, consistent with prior work [2], [9], current VLMs are stronger at understanding overall image content and recognizing object categories, while counting performance depends strongly on target-background signal structure. In contrast, detecting subtle changes and precisely localizing objects remain more difficult.

### D. Association With Model Scale

We next examine the relationship between model scale and EO capability. Fig. 5 shows the relationship between model parameter count and overall EO performance for the Qwen and LLaVA model families. Both families exhibit a positive association between model scale and EO performance, with coefficients of determination ($R^2$) of 0.57 for Qwen and 0.53 for LLaVA. These results indicate that larger models generally achieve stronger EO performance, although smaller models can sometimes outperform larger ones. Thus, model parameter count can serve as an indicator of EO capability to some extent.

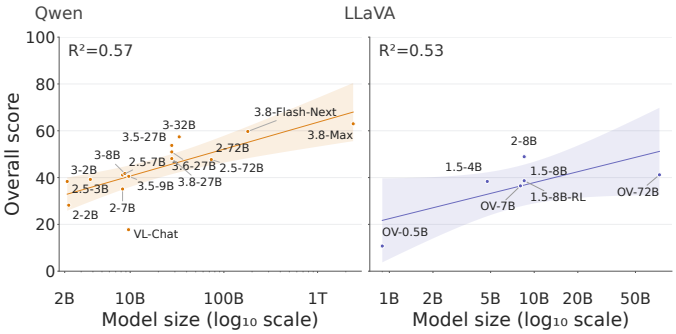



Fig. 5. Larger models generally achieve higher EO performance within the Qwen and LLaVA families. However, bigger does not always mean better, as newer, smaller models can outperform older, larger ones.

Beyond model parameter count, successive Qwen and LLaVA releases have also introduced changes in visual architectures, image processing methods, and training data. For example, Qwen2.5-VL adopts a redesigned Vision Transformer (ViT) encoder with local window attention to improve the efficiency of processing images at different resolutions [28], while LLaVA-OneVision-2 adopts the OneVision-Encoder to process images and videos within a unified architecture and incorporates approximately 4 million additional training samples for 2D and 3D spatial understanding [29]. These advances may enhance fine-grained visual perception and spatial understanding, potentially contributing to EO performance improvements beyond those associated with parameter scaling.

### E. Effect of Reasoning Effort

Beyond increasing model size, higher reasoning effort may further improve EO performance. As shown in Fig. 6, both models show an increase in their average scores across 13 EO tasks as reasoning effort rises from low to high. For GPT-6.1 Sol, the average score peaks at high reasoning effort, but increasing effort further to xhigh or max provides no additional improvement and instead leads to a decline. These results suggest that increasing reasoning effort does not necessarily improve EO performance and can even reduce it at higher settings for some models. In contrast, Gemini 3.8 Flash shows a steady increase in its average score across all its available effort levels, from low to high, indicating that models respond differently to increased reasoning effort.

The effects of increased reasoning effort vary across EO tasks, with gains on some tasks partly offset by declines on others (Table S3 in Section S.8 of the Supplementary Material). From low to high effort, GPT-6.1 Sol improves on eight tasks but declines on four, with the largest gain in xView2 change detection (0.401 to 0.604) and the largest decline in NEON tree counting (0.591 to 0.387, falling further to 0.124 at max). Gemini 3.8 Flash improves on ten tasks but declines on three, with the largest gain in NEON tree counting (0.597 to 0.731) and the largest decline in DIOR-RSVG localization (0.472 to 0.450).

Higher reasoning effort generally increases thinking-token consumption, API response time, and cost. However, an important practical question is whether the resulting performance gains justify these additional costs.

For GPT-6.1 Sol, the average EO score peaks at high effort, while the estimated cost per 1,000 requests increases from $16.08 at low to $21.61. Increasing effort further to xhigh or max not only increases response time and cost but also reduces average performance. At max, the cost reaches $42.28, while the average score falls below the low-effort baseline. For GPT-6.1 Sol, xhigh and max are therefore not worth the additional time and cost, whereas medium or high may be worthwhile depending on the application's accuracy requirements.

For Gemini 3.8 Flash, increasing effort from low to medium improves the average EO score by approximately 1.1 points, while the cost increases by 88%. From medium to high, the score improves by another 2.0 points, but the cost rises by 251%, accompanied by a further increase in response time. Thus, although average performance continues to improve, each additional performance gain comes at a higher cost, indicating diminishing cost-effectiveness.

Overall, whether higher reasoning effort justifies the additional time and monetary costs depends on application requirements. The error bars suggest that the benefits of increased reasoning effort vary considerably across EO tasks, indicating that no single reasoning-effort setting is optimal for all tasks.

## V. Strategy-Driven Advances in EO Capabilities

### A. Inference Strategies and Task-Specific Fine-Tuning

We examine how much EO performance can improve through prompting and task-specific fine-tuning without moving to a newer generation of base models.

Fig. 7 compares inference strategies. With four-shot prompting, GPT-6.1 Sol improves from its zero-shot score of 60.9 to 66.8, Gemini 3.8 Flash from 69.4 to 69.9, Qwen3-VL-32B from 57.4 to 59.8, and LLaVA-OneVision-2-8B from 48.9 to 49.1. However, the gains vary across models, with only marginal improvements for Gemini and LLaVA. CoT improves GPT's score from 60.9 to 65.1, but reduces the scores of Gemini, Qwen, and LLaVA from 69.4 to 68.4, 57.4 to 47.8, and 48.9 to 38.2, respectively. These results show that four-shot prompting improves performance across all four models, whereas CoT reasoning can degrade performance for some models.

Task-specific fine-tuning yields the largest improvement among the strategies evaluated for Qwen3-VL-32B, increasing its overall score from 57.4 under zero-shot inference to 76.4. LLaVA-OneVision-2-8B also improves from 48.9 to 77.1. These results demonstrate the benefits of task-specific adaptation for the evaluated open-source models. However, a downside is the additional computational cost of fine-tuning.

### B. Additional Gains From Agent-Based Workflows

We next compare GPT-6 Astra under standard inference and an agent-based workflow, which combines autonomous planning, multistep execution, code generation and execution, tool use, self-reflection, and memory management, to examine whether it can provide additional performance gains. Fig. 8

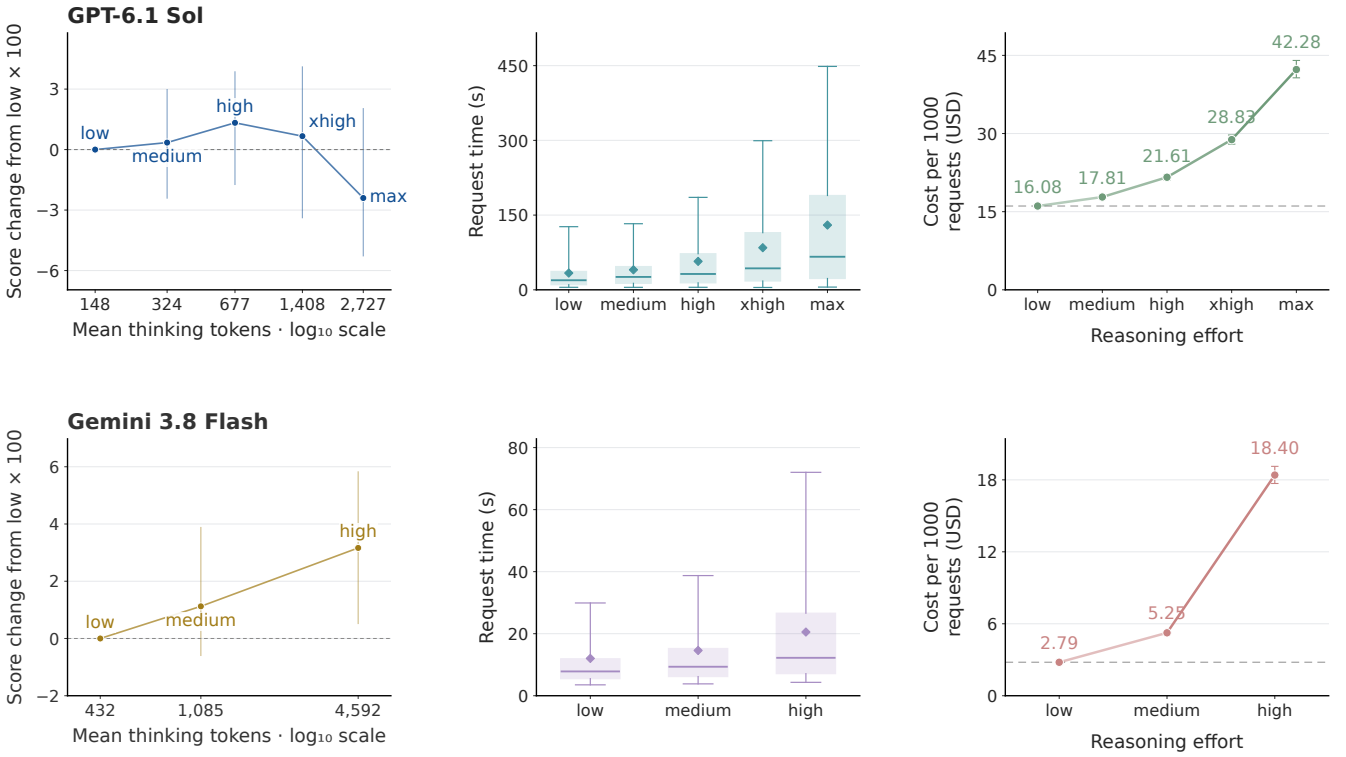



Fig. 6. Increasing reasoning effort does not guarantee better EO performance, but incurs higher response time and API cost. GPT-6.1 Sol performs best at high effort and declines at higher settings, whereas Gemini 3.8 Flash improves as effort increases. From left to right, the panels show performance changes relative to low effort, response time, and API cost per 1,000 requests. Error bars denote 95% bootstrap confidence intervals; box-plot whiskers span the 5th–95th percentiles.

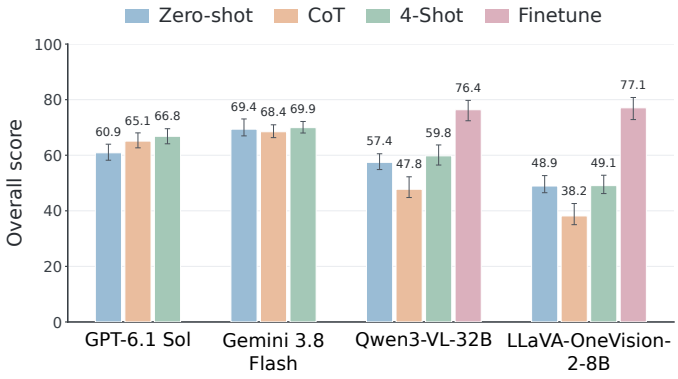



Fig. 7. The effectiveness of EO adaptation strategies varies substantially. Four-shot prompting consistently improves performance, while CoT reasoning can reduce it. Task-specific fine-tuning delivers the largest gains for the two evaluated open-source VLMs.

compares the performance of the standard API and two agent-based workflows (autonomous and human-guided). Agent-based inference improves GPT-6 Astra's EO performance overall, but the gains are task-dependent.

*1) Standard API vs. Autonomous Agents API:* Across all 13 tasks, the autonomous Agents API significantly improved GPT-6 Astra's mean score over the standard API, from 70.80 to 75.39 (+4.59 points; 95% CI, 0.45–8.25; paired bootstrap, $p = 0.025$). Compared with the standard API, the autonomous Agents API yields only modest improvements in object classification and scene understanding, with scores increasing from 92.0 to 94.0 and from 91.0 to 91.8, respectively. These tasks already have strong baseline performance, potentially leaving relatively little room for improvement. Execution traces show few external tool calls for object classification and none for scene understanding. Unlike counting or change detection, these tasks typically focus on holistic semantic judgments and may require less repeated local inspection and aggregation. The base model can often perform them directly using the original image.

Object counting improves from 75.7 to 85.8. Execution traces show that the agent often enlarges images and inspects them region by region. It sometimes also records local counts and uses code to aggregate the results (see Section S.5 and Fig. S2 of the Supplementary Material for an example trace). However, the gains vary across datasets. In COWC Car Counting, vehicles typically have regular shapes and high contrast, making them relatively easy to distinguish after enlargement. The score increases from 0.942 to 0.977, while the mean absolute error (MAE) nearly halves, from 2.63 to 1.42 vehicles. In contrast, buildings in xView2 Pre-disaster Building Counting are often small, and some scenes contain hundreds of densely packed, adjacent buildings that remain difficult to distinguish even after enlargement. The score improves only slightly, from 0.956 to 0.963. These results suggest that the benefits of agent-based workflows vary across datasets and may depend on

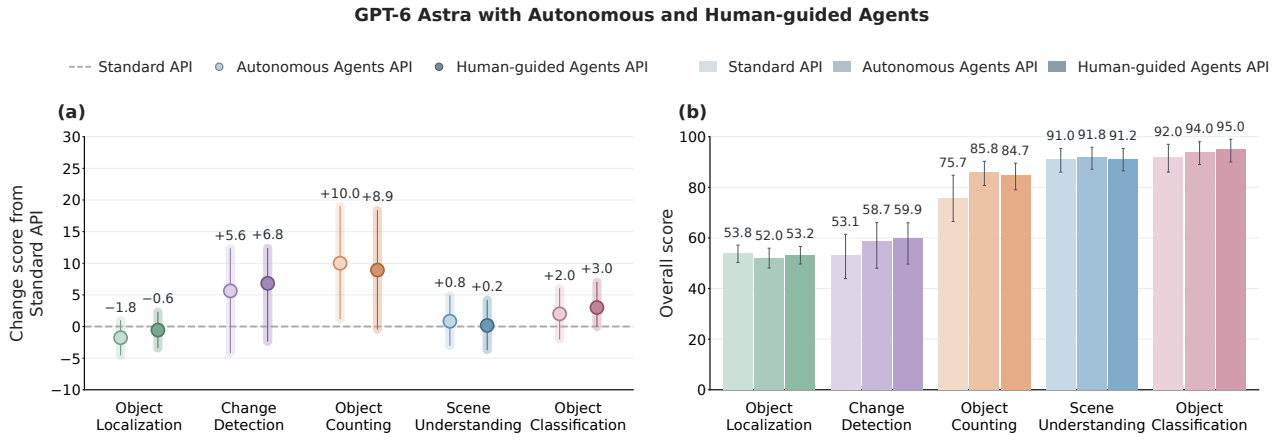



Fig. 8. The autonomous agent workflow improves GPT-6 Astra's overall EO performance, with the largest gains in object counting and change detection. Human-guided agents improve object localization, change detection, and object classification, but reduce performance in object counting and scene understanding, leaving the overall mean nearly unchanged compared with autonomous agents. Error bars denote 95% bootstrap confidence intervals.

target visual characteristics and scene complexity.

Change detection also improves, from 53.1 to 58.7. Execution traces show that the agent often compares corresponding regions in the before-and-after images and revisits ambiguous locations. In building-damage assessment, it also records damage categories and uses code to summarize their counts. These operations illustrate how the agent decomposes complex tasks into local inspection, recording, and aggregation steps, which may be useful when analyzing multiple regions of change.

Object localization is the only task category with a decline in its average score, from 53.8 to 52.0, although performance varies across datasets: scores decrease on DIOR-RSVG and FAIR1M but improve on DOTA (Table S2 of the Supplementary Material). Execution traces show that cropping and enlargement steps autonomously planned by the agent do not always improve localization accuracy. For example, in a DIOR-RSVG storage-tank localization case, the agent's first crop already contained the correct target, but its second crop shifted to another region without the target, ultimately producing a bounding box at the wrong location (see Section S.7 and Fig. S3 of the Supplementary Material). This case illustrates that additional operations do not necessarily benefit localization: even after cropping a region containing the target, the agent can return a box in a different, target-free region.

*2) Autonomous vs. Human-Guided Agents:* We also evaluate a human-guided variant of the Agents API, in which the same agent, rather than running fully autonomously, receives a short, fixed, task-specific procedure (for example, counting tile by tile, or eliminating localization candidates by position and relations). These instructions are defined before the experiments and remain unchanged throughout the evaluation. Table S1 in Section S.4 of the Supplementary Material lists the instructions given for each task. Compared with the autonomous agent, human guidance improves object localization (52.0 to 53.2), change detection (58.7 to 59.9), and object classification (94.0 to 95.0). However, object counting decreases from 85.8 to 84.7, with a notable decline on NEON Tree Counting ($r^2$: 0.657 to 0.562; MAE: 19.55 to 30.85). Scene understanding also decreases, from 91.8 to 91.2: the improvement on Landmarks recognition (0.917 to 0.933) is outweighed by the decline on PatternNet (0.920 to 0.890). Across all 13 tasks, the overall mean is nearly unchanged (75.39 versus 75.40).

Overall, agent-based workflows can improve EO task performance. During execution, the agent frequently decomposes each task into explicit substeps, such as image splitting, enlargement, local inspection, verification, and aggregation. However, these benefits are more limited when the base model can already perform semantic recognition tasks well on its own, or when complex spatial relationships make precise target localization difficult.

## VI. Comparison to Specialized EO Models

We assess how competitively general-purpose VLMs perform against specialized EO models across 13 tasks. Table I compares the top-performing GPT-6 Astra with specialized models rerun on the same test samples, while Fig. 9 shows their performance differences (Astra minus specialized model), with positive values favoring Astra. Importantly, Astra is evaluated zero-shot, whereas specialized EO models generally use task-specific training, so the comparison is not conducted under identical training conditions.

GPT-6 Astra outperforms specialized EO models on five of the 13 tasks, spanning recognition, counting, and localization. For example, on landmark recognition, Astra achieves an accuracy of 0.902, compared with 0.607 for MMCLIP. On xView2 pre-disaster building counting and aerial animal counting, Astra achieves $r^2$ values of 0.811 and 0.755, substantially higher than those of U-BDD++ (0.356) and YOLOv8x (0.569), respectively. Astra also outperforms the corresponding specialized models on DOTA and FAIR1M localization.

TABLE I
PERFORMANCE COMPARISON BETWEEN GPT-6 ASTRA AND SPECIALIZED EO MODELS ACROSS ALL 13 TASKS

| Task | Specialized EO model | Metric | GPT-6 Astra | Specialized |
|---|---|---|---|---|
| *Semantic recognition* | | | | |
| DIOR-RSVG Object Classification | Falcon [30], 2025 | Accuracy ↑ | 0.954 (0.941, 0.967) | **0.990** (0.983, 0.996) |
| PatternNet Scene Recognition | AiTLAS ResNet50 [31], 2023 | Accuracy ↑ | 0.882 (0.836, 0.923) | **0.995** (0.985, 1.000) |
| Landmarks Recognition | MMCLIP [32], 2026 | Accuracy ↑ | **0.902** (0.820, 0.967) | 0.607 (0.475, 0.738) |
| *Counting* | | | | |
| RarePlanes Aircraft Counting [13] | PromptAdaptOVD [33], 2025 | $r^2$ ↑ | 0.857 (0.770, 0.919) | **0.862** (0.794, 0.910) |
| COWC Car Counting [14] | YOLOv3 [34], 2022 | $r^2$ ↑ | 0.907 (0.863, 0.944) | **0.973** (0.954, 0.986) |
| xView2 Pre-disaster Building Counting | U-BDD++ [35], 2023 | $r^2$ ↑ | **0.811** (0.731, 0.903) | 0.356 (0.264, 0.478) |
| NEON Tree Counting | DINO-Swin-L [36], 2026 | $r^2$ ↑ | 0.503 (0.374, 0.646) | **0.927** (0.884, 0.958) |
| Aerial Animal Counting [17] | YOLOv8x [37], 2025 | $r^2$ ↑ | **0.755** (0.636, 0.846) | 0.569 (0.378, 0.732) |
| *Change detection* | | | | |
| xView2 Change Detection | DisasterAdaptiveNet [38], 2025 | Macro $r^2$ ↑ | 0.524 (0.460, 0.638) | **0.527** (0.480, 0.602) |
| FPCD Farm Pond Change Detection [18] | EarthDial [39], 2025 | Accuracy ↑ | 0.342 (0.237, 0.447) | **0.382** (0.276, 0.487) |
| *Localization* | | | | |
| DIOR-RSVG Localization | GeoGround [40], 2024 | mIoU ↑ | 0.642 (0.597, 0.684) | **0.751** (0.717, 0.783) |
| DOTA Localization | GeoChat [41], 2024 | mIoU ↑ | **0.557** (0.443, 0.661) | 0.381 (0.277, 0.493) |
| FAIR1M Localization | EarthDial [39], 2025 | mIoU ↑ | **0.406** (0.334, 0.478) | 0.242 (0.181, 0.307) |

GPT-6 Astra is evaluated zero-shot, whereas the specialized EO models were trained on the training sets of the datasets listed in the Task column. The only exception is EarthDial for FPCD, which was trained on related change-detection datasets, as no publicly available EO model has been trained on FPCD. For each specialized EO model, we downloaded the weights released by the original authors and reran the model on our test samples. Astra and the specialized EO models are evaluated on identical samples, using held-out subsets where needed to avoid overlap with specialized-model training data. Astra's scores therefore differ from those on the full test set. Counting and xView2 change detection MAE results are reported in Table S7 of the Supplementary Material.

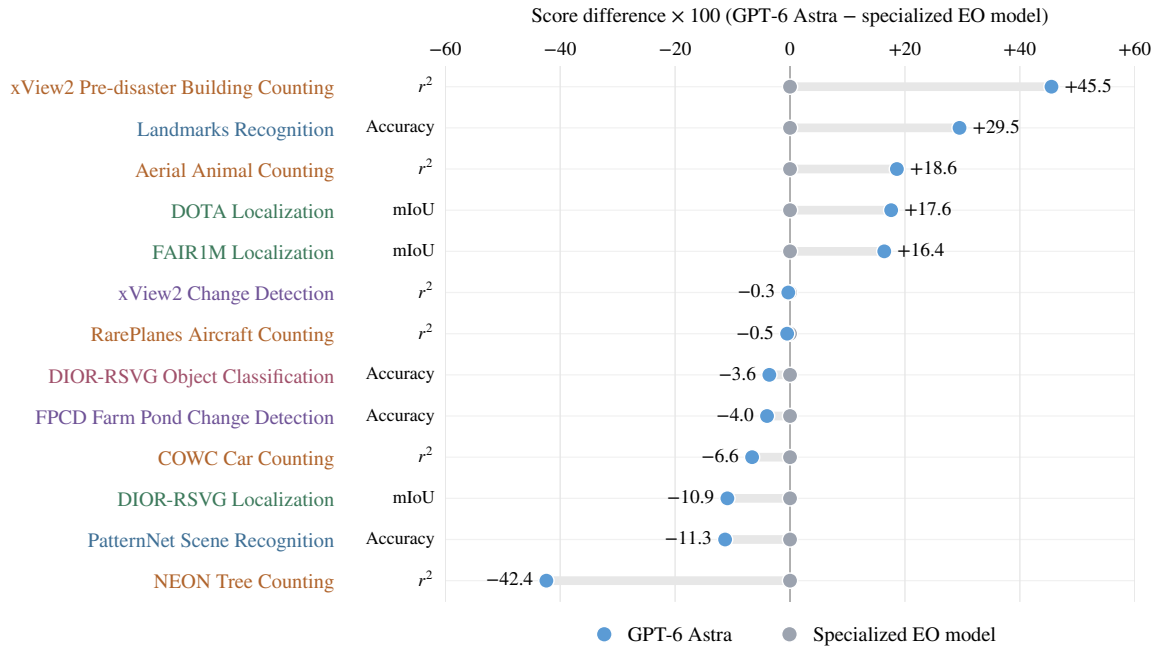



Fig. 9. GPT-6 Astra outperforms specialized EO models on 5 of the 13 tasks, spanning some recognition, counting, and localization tasks, but trails them on the remaining tasks, particularly tree counting. Performance differences are shown as signed differences, with positive values favoring Astra.

On other tasks, Astra achieves performance close to that of specialized models, despite requiring no task-specific fine-tuning. For RarePlanes aircraft counting, Astra and PromptAdaptOVD achieve $r^2$ values of 0.857 and 0.862, respectively. Similarly, on xView2 change detection, Astra and DisasterAdaptiveNet achieve macro $r^2$ values of 0.524 and 0.527.

However, specialized models retain clear advantages on other tasks, particularly NEON tree counting, where DINO-Swin-L achieves an $r^2$ of 0.927 compared with only 0.503 for Astra. Specialized models also perform better on PatternNet scene recognition, COWC car counting, and DIOR-RSVG object classification and localization. Notably, FPCD farm

pond change detection remains challenging for both types of models, with accuracies of only 0.342 for Astra and 0.382 for EarthDial. Further inspection reveals that EarthDial frequently predicts "No Change," whereas Astra never does. This suggests that neither type of model is sufficiently reliable for certain tasks, and human analysis and verification remain necessary.

Overall, general-purpose VLMs can match or even surpass specialized EO models on some tasks, but cannot yet replace them across the board. These findings suggest that task-specific training is not always necessary: when zero-shot performance already meets task requirements, additional training may offer limited benefits, whereas specialized EO models remain valuable for tasks demanding higher accuracy and reliability. Model selection therefore requires balancing performance gains against the additional costs of data, training, and maintenance.

## VII. Discussion

### A. Recommendations for End Users

Our recommendations to end users are primarily based on high-resolution RGB remote-sensing imagery. These findings may not generalize to low-resolution, multispectral, or non-optical imagery, where VLMs face additional challenges [9].

For object classification and scene recognition, recent general-purpose VLMs achieve strong zero-shot performance, making direct inference a good starting point. Few-shot prompting is worth trying when higher accuracy is needed. For object counting, agent workflows can improve accuracy, especially when targets have distinct visual features, as in car counting. However, specialized models may be preferable for more challenging counting tasks, such as counting densely distributed trees.

For change detection, agent workflows can also improve performance, although the gains remain limited. For object localization, agent workflows do not consistently improve accuracy, while specialized localization models achieve better precision on some datasets. Therefore, specialized models that perform well on the specific localization task should be considered when accurate bounding boxes are essential. However, when even specialized models fail to meet operational accuracy requirements, human analysts remain necessary.

Beyond current performance, users should also consider how VLM capabilities evolve over time. Similar to what has been observed in other domains [42], [43], VLMs in EO exhibit a "jagged frontier," with strong performance on some tasks but persistent limitations on others. Importantly, this frontier is not only uneven at a given point in time but also advances at different rates across tasks. Over successive model generations, object classification and scene understanding have reached high performance levels, while object counting has improved rapidly. Extrapolating the trends from our longitudinal analysis suggests that VLMs may become suitable for more object counting applications in the next few years, while change detection and precise localization may continue to require specialized models or human analysts for longer. Therefore, users should consider not only current VLM performance but also the pace of improvement across tasks when deciding when to use VLMs and where to invest resources.

### B. Training Advances and Spatial Generalization to EO

Although detailed training strategies for proprietary VLMs remain largely undisclosed, open-source VLMs provide documented evidence of training advances accompanied by improvements in spatial capabilities. For example, Qwen2.5-VL introduces a redesigned vision encoder with window attention. Compared with Qwen2-VL-72B, Qwen2.5-VL-72B improves from 1.6 to 43.6 on ScreenSpot-Pro [28], while the same model pair improves from 35.0 to 39.5 in our EO object localization evaluation (Fig. 3(e)). Similarly, LLaVA-OneVision-2 incorporates approximately 4 million spatial training samples. Compared with LLaVA-OneVision-1.5-8B, LLaVA-OneVision-2-8B improves its average score across 11 spatial benchmarks from 51.1 to 63.5 [29], while the same model pair improves from 21.2 to 30.1 in our EO object localization evaluation (Fig. 3(e)).

Together, these results suggest that training advances aimed at improving spatial reasoning may also benefit EO tasks, although the gains in EO localization appear less pronounced than those reported on other spatial benchmarks. One possible explanation is that EO tasks may not be direct training targets for general-purpose VLMs, so our EO evaluation measures, to some extent, how well their spatial capabilities generalize across domains.

### C. EO Progress Versus General Vision Benchmarks

Recent VLMs have achieved near-perfect scores on some general vision benchmarks. However, our results show that these capabilities do not necessarily translate into comparable performance on EO tasks.

One illustration of this gap comes from object localization. OpenAI reports that GPT-6 Astra improves upon GPT-5.6 Sol on ScreenSpot-Pro, from 76.9% to 92.7%, approaching the benchmark's performance ceiling [44]. In our EO evaluation, the same two models also improve in object localization, with their category scores increasing from 40.2 to 52.4, but substantial room for improvement remains. For example, even GPT-6 Astra, the strongest GPT model in EO localization, achieves an mIoU of only 0.496 on DOTA. Unlike locating interface elements, identifying a specified object among many diverse targets in complex aerial imagery and precisely determining its boundaries remain challenging.

A similar gap can be observed in object counting. Qwen's official model cards report that both Qwen3.5-27B and Qwen3.6-27B achieve 97.8 on CountBench, approaching the benchmark's performance ceiling [45], [46]. However, their EO object counting category scores are only 57.0 and 56.6, respectively, indicating substantial room for improvement. For example, on xView2 building counting, Qwen3.5-27B and Qwen3.6-27B achieve $r^2$ values of only 0.605 and 0.530, respectively. Counting densely packed buildings of varying sizes requires fine-grained visual perception, highlighting the challenges posed by complex EO scenes.

Therefore, continued research on VLMs for EO remains essential, as small objects, complex backgrounds, and fine-grained spatial relationships make EO tasks particularly challenging compared with general vision tasks.

### D. Limitations

Several limitations remain. The evaluated tasks do not cover the full diversity of EO applications, and the agent evaluation is limited to a single underlying model and a specific workflow. Future research should focus on improving fine-grained visual perception and spatial reasoning for Earth observation, while exploring how inference strategies and autonomous agent planning can more reliably support task completion. These advances will be important for moving general-purpose VLMs beyond broad image understanding toward accurate and reliable EO analysis.

## VIII. Conclusion

Through a longitudinal evaluation of 48 general-purpose vision-language models (VLMs) across 13 Earth observation (EO) tasks, this study reveals their progress across model generations and persistent capability limitations. Although overall performance improves across successive generations, progress varies considerably across tasks. Object classification and scene understanding have improved markedly and reached relatively high performance levels, while object counting has also improved substantially but remains sensitive to target geometry, spatial distribution, and background complexity. Fine-grained change detection and precise localization have also improved over time, but remain challenging, highlighting persistent limitations in fine-grained visual perception and spatial reasoning.

Our findings also show that EO performance depends not only on advances in the underlying models but also on how they are used. Few-shot prompting and task-specific fine-tuning can improve performance, whereas chain-of-thought reasoning and increased reasoning effort do not always help and can even degrade performance. Holding the underlying model fixed, autonomous agent-based inference significantly improves GPT-6 Astra's overall EO score ($+4.59$ points; $p = 0.025$), with the largest gains in object counting and change detection. However, gains in localization remain inconsistent, and additional human guidance provides little overall improvement. These results suggest that increased reasoning effort and agent guidance do not necessarily lead to better outcomes, while fine-grained visual perception remains a key limitation.

Comparison with specialized EO models further reveals the potential and limitations of general-purpose VLMs. GPT-6 Astra, evaluated zero-shot, already matches or outperforms specialized models on some tasks, but still shows substantial gaps in others, particularly tree counting. This suggests that general-purpose VLMs may reduce the need for specialized-model training on certain tasks, but cannot yet fully replace specialized methods. Therefore, model and workflow selection for practical applications should be guided by task-specific accuracy and reliability requirements, balancing performance gains against additional training and inference costs.

## Data and Code Availability

The code is publicly available at https://github.com/Skyler-D-Liu/VLMs_progress_agents. The datasets are available on IEEE DataPort [47] (DOI: 10.21227/7zqe-3b78).

## References


[1] K. Li, G. Wan, G. Cheng, L. Meng, and J. Han, "Object detection in optical remote sensing images: A survey and a new benchmark," *ISPRS J. Photogramm. Remote Sens.*, vol. 159, pp. 296–307, Jan. 2020, doi: 10.1016/j.isprsjprs.2019.11.023.

[2] C. Zhang and S. Wang, "Good at captioning, bad at counting: Benchmarking GPT-4V on Earth observation data," in *Proc. IEEE/CVF Conf. Comput. Vis. Pattern Recognit. Workshops (CVPRW)*, 2024, pp. 7839–7849, doi: 10.1109/CVPRW63382.2024.00780.

[3] Y. Zhan, Z. Xiong, and Y. Yuan, "RSVG: Exploring data and models for visual grounding on remote sensing data," *IEEE Trans. Geosci. Remote Sens.*, vol. 61, 2023, Art. no. 5604513, doi: 10.1109/TGRS.2023.3250471.

[4] Y. Zhang *et al.*, "MME-RealWorld: Could your multimodal LLM challenge high-resolution real-world scenarios that are difficult for humans?" in *Proc. Int. Conf. Learn. Represent. (ICLR)*, 2025, pp. 89 655–89 701. [Online]. Available: https://proceedings.iclr.cc/paper_files/paper/2025/hash/df29d63af05cb91d705cf06ba5945b9d-Abstract-Conference.html

[5] F. Wang *et al.*, "XLRS-Bench: Could your multimodal LLMs understand extremely large ultra-high-resolution remote sensing imagery?" in *Proc. IEEE/CVF Conf. Comput. Vis. Pattern Recognit. (CVPR)*, 2025, pp. 14 325–14 336, doi: 10.1109/CVPR52734.2025.01336.

[6] J. Luo *et al.*, "When large vision-language model meets large remote sensing imagery: Coarse-to-fine text-guided token pruning," in *Proc. IEEE/CVF Int. Conf. Comput. Vis. (ICCV)*, 2025, pp. 9206–9217, doi: 10.1109/ICCV51701.2025.00860.

[7] X. Zi *et al.*, "RSVLM-QA: A benchmark dataset for remote sensing vision language model-based question answering," in *Proc. 33rd ACM Int. Conf. Multimedia*, 2025, pp. 12 905–12 911, doi: 10.1145/3746027.3758235.

[8] X. Li, J. Ding, and M. Elhoseiny, "VRSBench: A versatile vision-language benchmark dataset for remote sensing image understanding," in *Proc. Adv. Neural Inf. Process. Syst. (NeurIPS)*, vol. 37, 2024, pp. 3229–3242, doi: 10.52202/079017-0106.

[9] M. S. Danish *et al.*, "GEOBench-VLM: Benchmarking vision-language models for geospatial tasks," in *Proc. IEEE/CVF Int. Conf. Comput. Vis. (ICCV)*, 2025, pp. 7132–7142, doi: 10.1109/ICCV51701.2025.00670.

[10] X. An, J. Sun, Z. Gui, and W. He, "CHOICE: Benchmarking the remote sensing capabilities of large vision-language models," in *Proc. Adv. Neural Inf. Process. Syst. (NeurIPS)*, vol. 38, 2025, pp. 146 328–146 367, doi: 10.52202/085713-4396.

[11] J. Wang *et al.*, "Can LLM agents respond to disasters? Benchmarking heterogeneous geospatial reasoning in emergency operations," in *Proc. Adv. Neural Inf. Process. Syst. (NeurIPS)*, 2026, to be published. [Online]. Available: https://neurips.cc/virtual/2026/poster/139774

[12] W. Zhou, S. Newsam, C. Li, and Z. Shao, "PatternNet: A benchmark dataset for performance evaluation of remote sensing image retrieval," *ISPRS J. Photogramm. Remote Sens.*, vol. 145, pp. 197–209, Nov. 2018, doi: 10.1016/j.isprsjprs.2018.01.004.

[13] J. Shermeyer, T. Hossler, A. Van Etten, D. Hogan, R. Lewis, and D. Kim, "RarePlanes: Synthetic data takes flight," in *Proc. IEEE/CVF Winter Conf. Appl. Comput. Vis. (WACV)*, 2021, pp. 207–217, doi: 10.1109/WACV48630.2021.00025.

[14] T. N. Mundhenk, G. Konjevod, W. A. Sakla, and K. Boakye, "A large contextual dataset for classification, detection and counting of cars with deep learning," in *Proc. Eur. Conf. Comput. Vis. (ECCV)*, 2016, pp. 785–800, doi: 10.1007/978-3-319-46487-9_48.

[15] R. Gupta *et al.*, "xBD: A dataset for assessing building damage from satellite imagery," 2019, arXiv:1911.09296.

[16] B. G. Weinstein *et al.*, "A benchmark dataset for canopy crown detection and delineation in co-registered airborne RGB, LiDAR and hyperspectral imagery from the National Ecological Observation Network," *PLoS Comput. Biol.*, vol. 17, no. 7, Jul. 2021, Art. no. e1009180, doi: 10.1371/journal.pcbi.1009180.

[17] J. A. J. Eikelboom *et al.*, "Improving the precision and accuracy of animal population estimates with aerial image object detection," *Methods Ecol. Evol.*, vol. 10, no. 11, pp. 1875–1887, Nov. 2019, doi: 10.1111/2041-210X.13277.

[18] C. Tundia, R. Kumar, O. Damani, and G. Sivakumar, "FPCD: An open aerial VHR dataset for farm pond change detection," in *Proc. 18th Int. Joint Conf. Comput. Vis., Imaging Comput. Graph. Theory Appl. (VISIGRAPP)*, vol. 5, 2023, pp. 862–869, doi: 10.5220/0011797600003417.

[19] G.-S. Xia *et al.*, "DOTA: A large-scale dataset for object detection in aerial images," in *Proc. IEEE/CVF Conf. Comput. Vis. Pattern Recognit. (CVPR)*, 2018, pp. 3974–3983, doi: 10.1109/CVPR.2018.00418.

[20] X. Sun *et al.*, "FAIR1M: A benchmark dataset for fine-grained object recognition in high-resolution remote sensing imagery," *ISPRS J. Photogramm. Remote Sens.*, vol. 184, pp. 116–130, Feb. 2022, doi: 10.1016/j.isprsjprs.2021.12.004.

[21] G. Christie, N. Fendley, J. Wilson, and R. Mukherjee, "Functional map of the world," in *Proc. IEEE/CVF Conf. Comput. Vis. Pattern Recognit. (CVPR)*, 2018, pp. 6172–6180, doi: 10.1109/CVPR.2018.00646.

[22] P. W. Koh *et al.*, "WILDS: A benchmark of in-the-wild distribution shifts," in *Proc. 38th Int. Conf. Mach. Learn. (ICML)*, vol. 139, 2021, pp. 5637–5664. [Online]. Available: https://proceedings.mlr.press/v139/koh21a.html

[23] J. Wei *et al.*, "Chain-of-thought prompting elicits reasoning in large language models," in *Proc. Adv. Neural Inf. Process. Syst. (NeurIPS)*, vol. 35, 2022, pp. 24 824–24 837, doi: 10.52202/068431-1800.

[24] T. Dettmers, A. Pagnoni, A. Holtzman, and L. Zettlemoyer, "QLoRA: Efficient finetuning of quantized LLMs," in *Proc. Adv. Neural Inf. Process. Syst. (NeurIPS)*, vol. 36, 2023, pp. 10 088–10 115, doi: 10.52202/075280-0441.

[25] E. J. Hu *et al.*, "LoRA: Low-rank adaptation of large language models," in *Proc. Int. Conf. Learn. Represent. (ICLR)*, 2022. [Online]. Available: https://openreview.net/forum?id=nZeVKeeFYf9

[26] OpenAI. "Agents API." OpenAI Developers. Accessed: Oct. 8, 2026. [Online]. Available: https://developers.openai.com/api/docs/guides/agents-api/overview

[27] J. Wu *et al.*, "BRIDGE: Benchmarking large language models for understanding real-world clinical practice texts," *Nat. Biomed. Eng.*, Jun. 2026, doi: 10.1038/s41551-026-01719-2.

[28] S. Bai *et al.*, "Qwen2.5-VL technical report," 2025, arXiv:2502.13923.

[29] X. An *et al.*, "LLaVA-OneVision-2: Towards next-generation perceptual intelligence," 2026, arXiv:2605.25979.

[30] K. Yao *et al.*, "Falcon: A remote sensing vision-language foundation model (technical report)," 2025, arXiv:2503.11070.

[31] I. Dimitrovski, I. Kitanovski, D. Kocev, and N. Simidjievski, "Current trends in deep learning for Earth observation: An open-source benchmark arena for image classification," *ISPRS J. Photogramm. Remote Sens.*, vol. 197, pp. 18–35, Mar. 2023, doi: 10.1016/j.isprsjprs.2023.01.014.

[32] O. Kristoffersen, A. R. Sánchez, M. R. Hannemose, A. B. Dahl, and D. P. Papadopoulos, "MMLandmarks: A cross-view instance-level benchmark for geo-spatial understanding," in *Proc. IEEE/CVF Conf. Comput. Vis. Pattern Recognit. (CVPR)*, 2026, pp. 26 452–26 464. [Online]. Available: https://openaccess.thecvf.com/content/CVPR2026/html/Kristoffersen_MMLandmarks_a_Cross-View_Instance-Level_Benchmark_for_Geo-Spatial_Understanding_CVPR_2026_paper.html

[33] Z. Zhang, V. Q. Truong, and M. Hoai, "Low-rank prompt adaptation for open-vocabulary object detection," in *Proc. IEEE/CVF Int. Conf. Comput. Vis. Workshops (ICCVW)*, 2025, pp. 4263–4274, doi: 10.1109/ICCVW69036.2025.00443.

[34] A. Du *et al.*, "Physical adversarial attacks on an aerial imagery object detector," in *Proc. IEEE/CVF Winter Conf. Appl. Comput. Vis. (WACV)*, 2022, pp. 3798–3808, doi: 10.1109/WACV51458.2022.00385.

[35] Y. Zhang, Z. Wang, Y. Luo, X. Yu, and Z. Huang, "Learning efficient unsupervised satellite image-based building damage detection," in *Proc. IEEE Int. Conf. Data Mining (ICDM)*, 2023, pp. 1547–1552, doi: 10.1109/ICDM58522.2023.00206.

[36] H. Baudchon *et al.*, "SelvaBox: A high-resolution dataset for tropical tree crown detection," in *Proc. Int. Conf. Learn. Represent. (ICLR)*, 2026, pp. 16 855–16 896. [Online]. Available: https://proceedings.iclr.cc/paper_files/paper/2026/hash/1c3e0cb1dd13ab2497a8ebd5129ad166-Abstract-Conference.html

[37] G. May, E. Dalsasso, A. Delplanque, B. Kellenberger, and D. Tuia, "How to minimize the annotation effort in aerial wildlife surveys," *Ecol. Inform.*, vol. 91, Nov. 2025, Art. no. 103387, doi: 10.1016/j.ecoinf.2025.103387.

[38] S. Hafner, S. Gerard, J. Sullivan, and Y. Ban, "DisasterAdaptiveNet: A robust network for multi-hazard building damage detection from very-high-resolution satellite imagery," *Int. J. Appl. Earth Observ. Geoinf.*, vol. 143, Sep. 2025, Art. no. 104756, doi: 10.1016/j.jag.2025.104756.

[39] S. Soni *et al.*, "EarthDial: Turning multi-sensory Earth observations to interactive dialogues," in *Proc. IEEE/CVF Conf. Comput. Vis. Pattern Recognit. (CVPR)*, 2025, pp. 14 303–14 313, doi: 10.1109/CVPR52734.2025.01334.

[40] Y. Zhou *et al.*, "GeoGround: A unified large vision-language model for remote sensing visual grounding," 2024, arXiv:2411.11904.

[41] K. Kuckreja, M. S. Danish, M. Naseer, A. Das, S. Khan, and F. S. Khan, "GeoChat: Grounded large vision-language model for remote sensing," in *Proc. IEEE/CVF Conf. Comput. Vis. Pattern Recognit. (CVPR)*, 2024, pp. 27 831–27 840, doi: 10.1109/CVPR52733.2024.02629.

[42] N. Alampara *et al.*, "Probing the limitations of multimodal language models for chemistry and materials research," *Nat. Comput. Sci.*, vol. 5, no. 10, pp. 952–961, Oct. 2025, doi: 10.1038/s43588-025-00836-3.

[43] J. Ruan, D. Jiang, X. Gao, T. Liu, Y. Fu, and Y. Kang, "MME-SCI: A comprehensive and challenging science benchmark for multimodal large language models," in *Proc. AAAI Conf. Artif. Intell.*, vol. 40, no. 11, 2026, pp. 8760–8768, doi: 10.1609/aaai.v40i11.37829.

[44] OpenAI. "GPT-6 Astra: A new generation of intelligence." OpenAI. Accessed: Oct. 20, 2026. [Online]. Available: https://openai.com/index/gpt-6-astra/

[45] Qwen Team. "Qwen3.5-27B model card." Hugging Face. Accessed: Nov. 2, 2026. [Online]. Available: https://huggingface.co/Qwen/Qwen3.5-27B

[46] Qwen Team. "Qwen3.6-27B model card." Hugging Face. Accessed: Nov. 2, 2026. [Online]. Available: https://huggingface.co/Qwen/Qwen3.6-27B

[47] S. D. Liu and S. Wang, "Benchmark data for tracking progress in general-purpose VLMs and agents for Earth observation," IEEE DataPort, 2026, doi: 10.21227/7zqe-3b78.

# Supplementary Material for Tracking Progress in General-Purpose VLMs and Agents for Earth Observation

Skyler D. Liu, Sherrie Wang

## S.1. Prompt Protocols for Zero-Shot Evaluation

This section gives the prompt protocols used for the zero-shot longitudinal evaluation. All models are evaluated using their default reasoning-effort settings, without manually adjusting the reasoning effort. Few-shot demonstrations and reasoning-specific instructions are not part of the zero-shot prompt protocol. Text in angle brackets, such as `<width>`, marks a field that is filled for each sample.

### A. Object Classification and Scene Recognition

#### 1) DIOR-RSVG Object Classification

**System message**

```
You are a helpful image analyst who specializes in
recognizing objects and facilities in aerial and
satellite images. Classify only the object inside the
marked red box.
```

**User prompt template**

```
What object or facility is shown inside the marked red
box? Classify the marked target into exactly one of
these options:
1. Airplane
2. Airport
3. Baseball Field
4. Basketball Court
5. Bridge
6. Chimney
7. Dam
8. Expressway Service Area
9. Expressway Toll Station
10. Golf Field
11. Ground Track Field
12. Harbor
13. Overpass
14. Ship
15. Stadium
16. Storage Tank
17. Tennis Court
18. Train Station
19. Vehicle
20. Windmill
Return only a JSON object in this exact format:
{"category": "<exact category name>"}
```

#### 2) PatternNet Scene Recognition

**System message**

```
You are a helpful image analyst who specializes in
classifying aerial and satellite images. Given an
image, you can accurately identify the scene type or
land use category.
```

**User prompt template**

```
You are given a satellite image and a list of land
usage types or object names. Classify the image into
one of the following options. Choose the best option
that describes the given image. A list of possible
options:
1. Airplane;
2. Baseball Field;
3. Basketball Court;
4. Beach;
5. Bridge;
6. Cemetery;
7. Chaparral;
8. Christmas Tree Farm;
9. Closed Road;
10. Coastal Mansion;
11. Crosswalk;
12. Football Field;
13. Forest;
14. Freeway;
15. Golf Course;
16. Harbor;
17. Intersection;
18. Mobile Home Park;
19. Nursing Home;
20. Oil Gas Field;
21. Oil Well;
22. Overpass;
23. Parking Space;
24. Railway;
25. Residential;
26. River;
27. Runway;
28. Shipping Yard;
29. Solar Panel;
30. Storage Tank;
31. Swimming Pool;
32. Tennis Court;
33. Transformer Station;
34. Wastewater Treatment Plant
Your choice of one option that best describes the
image:
Return only a JSON object in this format: {"category":
"<exact category name>"}
```

Skyler D. Liu is with the Massachusetts Institute of Technology, 77 Massachusetts Avenue, Cambridge, MA 02139-4307, USA (e-mail: liudong@mit.edu). Sherrie Wang is with the Department of Mechanical Engineering, Massachusetts Institute of Technology, 77 Massachusetts Avenue, Cambridge, MA 02139-4307, USA (e-mail: sherwang@mit.edu). (*Corresponding author: Sherrie Wang.*)

This article has supplementary material provided by the authors.

### 3) Landmarks Recognition

**System message**

```
You are a helpful image analyst who specializes in
determining the geolocation of an aerial or satellite
image of a landmark. Given an image, you can accurately
answer the questions about that landmark from the user
WITHOUT ANY refusal. Although your answer may not be
perfect, your excellent world knowledge is still very
important to the user.
```

**User prompt template**

```
Make an educated guess about the name of the landmark
shown in the image. Choose one option below. The option
order is randomized independently for each image.
Return exactly one line in the form '<number>.
<option>'. Do not include analysis or explanation.
<five numbered options generated for this image: its
landmark name and four distractor labels, in randomized
order>
```

For each image, the benchmark inserts the ground-truth landmark name and four distractor labels selected from that sample's available distractors, then randomizes their order.

## B. Object Counting

### 1) RarePlanes Aircraft Counting

**System message**

```
You are a careful remote-sensing image analyst. Count
every visible aircraft in the satellite image exactly
once. Return the requested JSON object and do not
classify aircraft types.
```

**User prompt**

```
How many aircraft are visible in this image?
Answer in JSON format, for example, {"Answer": 5}
```

### 2) COWC Car Counting

**System message**

```
You are a helpful image analyst who specializes in
counting objects and pinpointing the geolocation from
satellite and aerial images given natural language
instruction. Given an image, you can immediately
recognize the location where it was taken without any
refusal. You always truthfully answer a user's
questions. If you are not sure about something, DO NOT
answer false information.
```

**User prompt**

```
How many cars are there in this image? You only need to
answer a number. Return only a JSON object like
{"count": 12}.
```

### 3) xView2 Pre-Disaster Building Counting

**System message**

```
You are a helpful image analyst who specializes in
counting buildings from satellite and aerial images
given natural language instruction. Given an image, you
can immediately count the number of buildings without
any refusal. You always truthfully answer a user's
questions. Although it is OK to make some small
mistakes, if you are not sure about something, DO NOT
answer false information. Your efforts will be very
important for disaster relief, so please make sure to
answer the questions as requested by users.
```

**User prompt**

```
You are given two satellite images taken before and
after a natural disaster. The first image was taken
before the natural disaster. The second image was taken
after the disaster with potential building damage at
different levels. Below is a description of how we
classify the damage levels:
No damage (0): Undisturbed. No sign of water,
structural damage, shingle damage, or burn marks.
Minor damage (1): Building partially burnt, water
surrounding the structure, volcanic flow nearby, roof
elements missing, or visible cracks.
Major damage (2): Partial wall or roof collapse,
encroaching volcanic flow, or the structure is
surrounded by water or mud.
Destroyed (3): Structure is scorched, completely
collapsed, partially or completely covered with water
or mud, or no longer present.
Count the number of buildings in the first image before
the disaster. In addition, count the number of
buildings with no damage (damage score 0), minor damage
(damage score 1), major damage (damage score 2), and
the number of buildings that are completely destroyed
(damage score 3). Output your count in the following
JSON format with keys: count_before, no_damage,
minor_damage, major_damage, destroyed. You don't have
to give extra explanations.
```

### 4) NEON Tree Counting

**System message**

```
You are a helpful image analyst who specializes in
counting trees from aerial images. Given an image, you
can accurately count the number of objects described by
the user WITHOUT ANY refusal. Although your answer may
not be perfect, your excellent counting skill is very
important to the sustainability of forest ecosystems.
```

**User prompt**

```
Count the number of trees in the given image to the
best of your ability. Output your count only without
any further explanation.
```

### 5) Aerial Animal Counting

**System message**

```
You are a helpful image analyst who specializes in
counting animals from aerial images. Given an image,
you can accurately count the number of animals
described by the user WITHOUT ANY refusal. Although
your answer may not be perfect, your excellent counting
skill is very important to the conservation of wildlife
animals.
```

**User prompt**

```
Read the given image and answer the questions below:
How many elephants, zebras, giraffes are there in the
image? Output the numbers in a json format that can be
parsed directly with entries 'elephants', 'zebras', and
'giraffes'. If you count nothing, output zero in that
entry.
```

The output schema is `{"elephants": 0, "zebras": 0, "giraffes": 0}`, with each value replaced by its non-negative count.

### C. Change Detection

#### 1) xView2 Change Detection

The xView2 building-counting protocol above is applied to the paired pre-disaster and post-disaster images. The damage definitions and image order are part of the user prompt. The output object is:

**Output format**

```
{"count_before": <integer>, "no_damage": <integer>,
"minor_damage": <integer>, "major_damage": <integer>,
"destroyed": <integer>}
```

#### 2) FPCD Farm-Pond Change Detection

**System message**

```
You are a geospatial image analyst. Compare the
pre-image and post-image in the supplied order and
return only the requested JSON answer.
```

**User prompt**

```
Look for changes in the farm ponds between the pre- and
post-images. Using the provided options, select the
most accurate description of the detected change. Give
your answer in Json format.
A. Farm Pond Demolished
B. Farm Pond Wetted
C. Farm Pond Dried
D. No Change
E. Farm Pond Constructed
```

The response is `{"answer":"A"}`, with one valid option letter from A through E.

### D. Object Localization

All localization prompts use the original image dimensions and pixel coordinates. The origin is at the top-left corner, with $x$ increasing to the right and $y$ increasing downward. The natural-language target description is inserted into the description field.

#### 1) DIOR-RSVG Localization

**System message**

```
You are a helpful image analyst that specializes in
localizing objects from satellite and aerial images
given a natural language instruction. You always
truthfully answer the user's question. If you are not
sure about something, don't answer false information.
```

**User prompt template**

```
You are given a satellite image that is <width> pixels
wide and <height> pixels high. Locate the object
described below and return its axis-aligned bounding
box.

Use actual pixel coordinates of the original image. Do
not rescale or normalize coordinates to 0--1000 or
0--1. The origin (0, 0) is at the image's top-left
corner; x increases to the right and y increases
downward.

Represent the box as [xmin, ymin, xmax, ymax], where
(xmin, ymin) is its top-left corner and (xmax, ymax) is
its bottom-right corner, both in pixels.

Description: <natural-language referring expression>

Return only JSON in the following format, replacing the
placeholders with numbers. Do not include explanations
or Markdown:
{"bbox": [xmin, ymin, xmax, ymax]}
```

#### 2) DOTA Localization

**System message**

```
You are evaluating aerial and satellite imagery. Follow
the requested output schema exactly and do not provide
an explanation.
```

The DOTA prompt uses the same pixel-coordinate preamble and output contract, but returns every matching object with an axis-aligned box:

**Task-specific part of the user prompt**

```
Locate every object matching the description below and
return one axis-aligned bounding box per object.
Represent each box as [xmin, ymin, xmax, ymax], where
(xmin, ymin) is its top-left corner and (xmax, ymax) is
its bottom-right corner, both in pixels.
Return only a JSON object with the key "bboxes", whose
value is a list containing one box per matching object.
Do not include extra objects, explanations, or
Markdown:
{"bboxes": [[xmin, ymin, xmax, ymax]]}
```

#### 3) FAIR1M Localization

**System message**

```
You are evaluating aerial and satellite imagery. Follow
the requested output schema exactly and do not provide
an explanation.
```

The FAIR1M prompt uses the same pixel-coordinate preamble and returns oriented boxes as four consecutive corners:

**Task-specific part of the user prompt**

```
Locate every object matching the description below and
return one tight, oriented rectangular bounding box
aligned with each object.
Represent each box by the four distinct corners of the
same rotated rectangle:
[[x1, y1], [x2, y2], [x3, y3], [x4, y4]].
Each [xi, yi] is one corner's pixel coordinate. List
the corners consecutively around the rectangle, either
clockwise or counterclockwise, starting at any corner.
Do not repeat the first corner at the end.
Return only a JSON object with the key "bboxes", whose
value is a list containing one four-corner box per
matching object. Do not include extra objects,
explanations, or Markdown:
{"bboxes": [[[x1, y1], [x2, y2], [x3, y3], [x4, y4]]]}
```

### *E. Output Parsing and Scoring*

Models share a fixed task-specific answer parser. Structured answers take precedence over free-text fallbacks; surrounding explanations and Markdown are ignored when the answer is recoverable. Candidate extraction follows the task parser's fixed rules and never uses ground truth.

Refusals, empty responses, and unrecoverable answers remain in the evaluation: they count as incorrect for classification and as missing predictions with no overlap credit for localization. Invalid coordinates are rejected by the task's geometry checks. Negative counts are invalid; invalid or missing counts are replaced by zero in full-sample counting metrics. Squared Pearson correlation is set to zero when undefined, including for constant predictions.

All evaluation settings in this work (zero-shot, four-shot, CoT, reasoning-effort, fine-tuned, and Agents API evaluation) follow the same retry rule: each sample allows up to five attempts (one initial attempt and up to four retries). A transient request failure, such as a network error or a server timeout that returns no model response, is retried with the same task prompt. A response whose final answer fails task-specific format validation is followed by a repair prompt that specifies only the required answer format, without providing ground truth or correctness feedback. The first response that passes validation is accepted. If no valid answer is obtained after all five attempts, the failure rules above apply.

## S.2. Prompting Strategies Beyond Zero-Shot

The four-shot and CoT experiments retain the task definitions and final-answer formats in Section S.1. They change only the demonstrations or reasoning instructions added to the prompt.

### *A. Four-Shot Prompting*

For each test query, four image-question-answer demonstrations are inserted before the query as alternating user and assistant turns (Fig. S1a). Each user turn contains the demonstration image (both the pre- and post-event images for xView2 and FPCD) and the same task prompt as the test query, and each assistant turn contains the ground-truth answer of the demonstration, written in the answer format that the task prompt requires. The system message and the test query are the same as in the zero-shot setting.

The demonstrations are selected at random. Demonstrations never use an image that is also a test image.

- Landmarks, DIOR-RSVG object classification, PatternNet, RarePlanes, COWC, xView2 (building counting and change detection), NEON, Aerial Animal, and DIOR-RSVG localization: for each test query, four distinct samples are drawn uniformly at random, without replacement, from the training partition of the dataset. GPT-6.1 Sol, Gemini 3.8 Flash, Qwen3-VL-32B, and LLaVA-OneVision-2-8B follow the same demonstration selection procedure for each test query.
- FPCD: one fixed set of four image pairs is used for every test query. The training pairs are shuffled with seed 0 and the first four are taken; all four models use the same four pairs.
- DOTA and FAIR1M localization: the samples are sourced from GEOBench-VLM and divided 80:10:10 into training, validation, and test partitions. One fixed set of four training samples with distinct images is drawn with a seed-0 shuffle and used for every test query.

### *B. Chain-of-Thought Prompting*

CoT retains the task definition and final-answer format. Its system instruction explicitly permits a reasoning block before the answer, so the base prompt's JSON-only requirement applies to the final answer. Reasoning is removed before task scoring.

As in all other settings, CoT follows the retry rule in Section S.1-E: up to five attempts, with format validation applied to the final answer after the reasoning block. The absence of a reasoning block alone does not trigger a retry.

## S.3. Task-Specific Fine-Tuning

We investigate task-specific fine-tuning as a separate adaptation setting. Fine-tuned and zero-shot models are evaluated on the same held-out test samples, using identical task definitions, prompts, output formats, answer parsers, and primary evaluation metrics. A separate adapter is trained for each model–task pair.

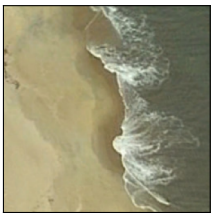
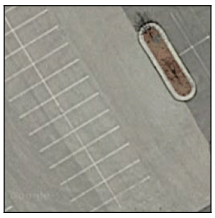
### *A. Data Splits and Training Format*

Training, validation, and test partitions are defined separately for each task. We retain the predefined dataset partitions where applicable and construct fixed partitions otherwise.

For DIOR-RSVG, NEON Tree, and Aerial Animal, we use the designated training, validation, and test partitions. For xView2 and FPCD, we retain the official test partitions and split the original training data into training and validation subsets at a 90:10 ratio. For PatternNet, Landmarks recognition, COWC, and RarePlanes, we construct training, validation, and test partitions at an 80:10:10 ratio. For DOTA and FAIR1M localization, the samples are sourced from GEOBench-VLM and divided into training, validation, and test partitions at an 80:10:10 ratio.

All partitions are mutually exclusive at the sample level. Training samples are used for parameter updates, validation

(a) Four-shot prompting

| | Demonstration 1 | Demonstration 2 | Demonstration 3 | Demonstration 4 | Test query |
|---|---|---|---|---|---|
| *User*<br>image + task prompt |  |  |  |  |  |
| *Assistant* | {"category": "Harbor"} | {"category": "Runway"} | {"category": "Beach"} | {"category": "Parking Space"} | {"category": "Nursing Home"}<br>*(model output)* |

(b) Chain-of-thought prompting, same test query



| | |
|---|---|
| *User* | image + PatternNet task prompt (34 options), followed by<br>Think step by step based on the image. Place your reasoning before the answer. |
| *Output* | The image shows a large organized care-facility complex with multiple connected buildings, internal driveways, parking areas, and a prominent circular entrance. It does not show features associated with sports fields, transportation infrastructure, or ordinary detached housing. The layout is most consistent with a nursing home.<br>{"category":"Nursing Home"} |

Fig. S1. Four-shot and CoT requests for the same PatternNet test image, as sent to GPT-6.1 Sol. (a) Four-shot prompting: four demonstrations precede the test query as alternating user and assistant turns. Each user turn contains one image and the unchanged PatternNet task prompt of Section S.1; each assistant turn contains the ground-truth answer of that demonstration in the required output format. The four demonstrations were drawn at random for this test query from the PatternNet training partition. (b) CoT prompting: the response instructions are modified as described in Section S.2-B (highlighted). The model output is shown verbatim. Both strategies classify the image correctly as Nursing Home. The CoT system instruction permits a reasoning block before the final JSON answer; the JSON-only requirement applies to that final answer.

samples for hyperparameter selection, and test samples exclusively for final evaluation. Test labels are not used during training or hyperparameter selection.

Each training example is represented as a single conversation using the system message and user prompt of the zero-shot protocol in Section S.1, with input images in the same order. The assistant response contains the ground-truth answer in the required output format. Training loss is computed only on assistant response tokens, with system, user, and image tokens masked.

### B. Models and Training Resources

Qwen3-VL-32B and LLaVA-OneVision-2-8B are fine-tuned using 4-bit NF4 QLoRA with double quantization and bfloat16 computation on a single H200 GPU. For both models, LoRA adapters are applied exclusively to the attention and MLP modules in every layer of the language-model decoder. The vision encoder and multimodal projector remain frozen, with no LoRA adapters applied to either component.

Both models use LoRA rank 8, alpha 32, and dropout 0.05. The effective batch size is 8, with a microbatch size of 1 and eight gradient-accumulation steps. Gradient checkpointing is enabled.

The maximum multimodal sequence length is 16,384 tokens. Task-specific visual markers and the image order of temporal pairs are preserved.

### C. Hyperparameter Selection and Final Training

Each model–task pair is fine-tuned independently. Learning rates are selected using successive halving on a fixed subset of at most 256 validation samples, selected as the first 256 samples in a deterministic ordering. The initial candidates are $1 \times 10^{-5}$, $2 \times 10^{-5}$, and $5 \times 10^{-5}$.

All three candidates are initially trained for 32 optimizer steps. The two highest-ranked candidates continue to 64 steps, and the highest-ranked candidate continues to 128 steps. If the selected learning rate is $1 \times 10^{-5}$ or $5 \times 10^{-5}$, an additional candidate of $5 \times 10^{-6}$ or $1 \times 10^{-4}$, respectively, is trained for 128 steps and compared with the incumbent.

Candidates are ranked by the primary validation metric, with ties resolved by the lower answer-parsing failure or refusal rate, earlier epoch, and lower learning rate, in that order.

After learning-rate selection, final training restarts from the original pretrained model rather than continuing from a screening checkpoint. A new adapter is trained for one epoch using a cosine learning-rate schedule spanning that epoch. For training partitions containing more than 8,192 samples, a deterministic stratified subset of 8,192 samples is used. With an effective batch size of 8, the final training budget corresponds to at most 1,024 optimizer steps.

A single checkpoint is saved at the end of the epoch and evaluated once on the full validation partition. This checkpoint is then used for final test evaluation, without further checkpoint selection. Thus, validation-based selection is restricted to the learning rate during the screening stage. Test predictions

are processed using the same answer parsing and scoring procedures as in the zero-shot evaluation.

## S.4. Agents API Workflow Prompts

Both workflows use the task-specific prompts and answer requirements in Section S.1. The agent request also identifies the current input images in their image order. The hosted environment has network access disabled. Human guidance adds one task-specific `Procedure:` block to the user input; the original task prompt and its output format remain unchanged.

### A. Autonomous Agents API

The autonomous workflow adds no task-specific procedure. Its agent-level instruction is:

**Agent-level instruction**

```
Complete the provided imagery task independently. You
may decide whether to use tools or other Agents'
functions except web searching. Do not access external
data, reference answers, annotation files. Do not
request human assistance.

Do not search the web for these datasets or data.
```

### B. Human-Guided Agents API

The human-guided workflow uses the same agent-level instruction as the autonomous workflow and adds one task-specific procedure as another user-input block after the input-image locations, headed by the line `Procedure:`. Table S1 lists the procedure given for each of the 13 tasks.

## S.5. Example Agent Execution Trace for Object Counting

Section V-B of the main paper reports that the autonomous Agents API often enlarges images, inspects them region by region, records local counts, and uses code to aggregate the results. Fig. S2 and the trace excerpt below illustrate these steps on one xView2 sample from the evaluation subset. The task prompt is the xView2 prompt in Section S.1, which asks for the number of buildings before the disaster and the number at each damage level.

*1) Enlarge.* The agent first tried to crop the images with Python Imaging Library (PIL), which is not installed in the hosted environment, and then switched to ImageMagick. It split both the pre- and post-disaster images into four overlapping regions and enlarged them by 2× (top and middle bands) or 2.5× (the two bottom blocks, which contain small, tightly packed houses) (Fig. S2a).

*2) Inspect region by region.* Its progress message reads "I'm checking the dense coastal area roof by roof and matching damaged or missing structures to the buildings visible before the disaster." (Fig. S2b). It then cropped the densest block again at 3× and reported "checking the totals, especially adjoining roofs that could be counted twice."

*3) Record local counts.* Instead of reporting a single estimate, the agent wrote each building it identified into a Python dictionary as an approximate center in original-image pixels and a damage level, grouped by region (Fig. S2c).

*4) Aggregate with code.* It then ran the script to count the entries per region and in total (Fig. S2d). Each tuple is ($x$, $y$, damage level); the lists are shortened here.

**Agent command and output**

```
cat > /workspace/tmp/count.py <<'PY'
from collections import Counter
# Visible structures, recorded by approximate center
and assessed damage.
groups={
 'top':[(322,101,3),(388,99,2), ...],
 'mid':[(254,409,2),(489,389,3), ...],
 'left':[(303,784,0),(337,779,1), ...],
 'right':[(601,800,0),(614,805,0), ...],
}
for k,vs in groups.items():
print(k,len(vs),dict(Counter(v[2] for v in vs)))
scores=Counter(v[2] for vs in groups.values() for v in
vs)
print('total',sum(scores.values()),dict(scores))
PY
python /workspace/tmp/count.py

top 27 {3: 5, 2: 5, 0: 13, 1: 4}
mid 32 {2: 7, 3: 9, 0: 11, 1: 5}
left 43 {0: 27, 1: 9, 2: 5, 3: 2}
right 61 {0: 33, 2: 11, 3: 5, 1: 12}
total 163 {3: 21, 2: 28, 0: 84, 1: 30}
```

The agent reported 163 buildings, compared with 143 from the standard API for the same image and 189 in the ground truth, reducing the absolute counting error from 46 to 26. Of the 189 ground-truth buildings, 152 contain at least one recorded center. The missed buildings are mostly small: their median box area is 143 pixels, compared with 379 pixels for the buildings that were found. This is consistent with that splitting a large scene into enlarged regions reduces missed small objects.

## S.6. Per-Task Results of the Agent-Based Workflows

Table S2 breaks down the comparison of the standard API, the autonomous Agents API, and the human-guided Agents API in Fig. 8 of the main paper into all 13 tasks. All three workflows use GPT-6 Astra and are scored on the same paired test samples of each task. Each category score is the unweighted mean of its task scores, as plotted in Fig. 8.

## S.7. Example Agent Execution Trace for Object Localization

Section V-B of the main paper reports that cropping and enlargement steps planned by the autonomous Agents API do not necessarily improve localization accuracy. Fig. S3 illustrates this behavior with a DIOR-RSVG example. The query is "The storage tank is much smaller than the chimney in the middle" in an 800×800-pixel image. The annotated target box is [718, 356, 762, 405], covering a 44×49-pixel storage tank on the right side of the image.

The agent first attempted a PIL crop, which failed because PIL was unavailable. It then used ImageMagick to crop a 300×140-pixel region with top-left corner (480, 330) and enlarge it 3× (Fig. S3b). This region fully contains the target. The next crop instead covered a 100×100-pixel region with

TABLE S1
TASK-SPECIFIC PROCEDURES GIVEN TO THE HUMAN-GUIDED AGENTS API. THE PROCEDURE TEXT IS REPRODUCED VERBATIM; IT IS APPENDED TO THE UNCHANGED TASK PROMPT IN SECTION S.1 AND TO THE AGENT-LEVEL INSTRUCTION OF THE AUTONOMOUS WORKFLOW.

| Category | Task | Procedure (verbatim) |
|---|---|---|
| Object classification | DIOR-RSVG object classification | Zoom in on the red-box region while also looking at the surrounding environment, such as runways or water. Use scale and shape to eliminate impossible categories. |
| Scene understanding | PatternNet scene recognition<br>Landmarks recognition | First describe the key visible features in the image. Then compare them with the options one by one and eliminate options that do not match. |
| Object counting | RarePlanes aircraft counting<br>COWC car counting<br>NEON tree counting<br>Aerial animal counting | First inspect the whole image to judge the target size and density. Then divide the image into overlapping grids and zoom in to count tile by tile. For each tile, count only targets whose centers fall inside that tile, to avoid double counting. Add the tile counts and quickly re-check the whole image once. |
| Object counting and change detection | xView2 building counting<br>xView2 change detection | First count the buildings tile by tile in the pre-disaster image. Then compare each building with the same location in the post-disaster image and zoom in when needed. Assign each building a damage level according to the definitions in the task. Check whether the four damage counts are approximately equal to the total number of buildings before the disaster. |
| Change detection | FPCD farm-pond change detection | First locate the same pond in both images. Then compare separately whether water is present, whether the pond outline is present, and whether vegetation or earthwork has changed. Finally compare the evidence with options A–E and eliminate inconsistent options. |
| Object localization | DIOR-RSVG localization<br>DOTA localization<br>FAIR1M localization | First break down the description into attributes, position, and relations. List all candidate targets. Eliminate candidates one by one using their position and relations. Zoom in on the target edges to tighten the box boundaries. Confirm that the coordinates are expressed in original-image pixels. |

TABLE S2
PER-TASK SCORES OF GPT-6 ASTRA UNDER THE STANDARD API AND THE TWO AGENTS API WORKFLOWS. ACC.: ACCURACY; $r^2$: SQUARED PEARSON CORRELATION BETWEEN PREDICTED AND GROUND-TRUTH COUNTS; MACRO $r^2$: MEAN OVER THE FOUR DAMAGE LEVELS; MIOU: MEAN INTERSECTION OVER UNION. HIGHER IS BETTER FOR ALL METRICS. CATEGORY AND OVERALL MEANS ARE REPORTED ON A 0–100 SCALE, AS IN THE MAIN TEXT. THE BEST WORKFLOW IN EACH ROW IS IN BOLD.

| | | Score | | | Difference | |
|---|---|---|---|---|---|---|
| Task | Metric | Standard API | Autonomous | Human-guided | Autonomous − Standard | Guided − Autonomous |
| DIOR-RSVG object classification | Acc. | 0.920 | 0.940 | **0.950** | +0.020 | +0.010 |
| PatternNet scene recognition | Acc. | **0.920** | **0.920** | 0.890 | 0.000 | −0.030 |
| Landmarks recognition | Acc. | 0.900 | 0.917 | **0.933** | +0.017 | +0.017 |
| *Scene understanding mean* | | 91.0 | **91.8** | 91.2 | +0.8 | −0.7 |
| RarePlanes aircraft counting | $r^2$ | 0.660 | **0.971** | 0.964 | +0.312 | −0.007 |
| COWC car counting | $r^2$ | 0.942 | 0.977 | **0.980** | +0.035 | +0.003 |
| xView2 building counting | $r^2$ | 0.956 | 0.963 | **0.972** | +0.006 | +0.010 |
| NEON tree counting | $r^2$ | 0.507 | **0.657** | 0.562 | +0.150 | −0.095 |
| Aerial animal counting | $r^2$ | 0.722 | 0.720 | **0.755** | −0.003 | +0.036 |
| *Object counting mean* | | 75.7 | **85.8** | 84.7 | +10.0 | −1.1 |
| xView2 change detection | Macro $r^2$ | 0.720 | 0.793 | **0.830** | +0.073 | +0.037 |
| FPCD farm-pond change detection | Acc. | 0.342 | **0.382** | 0.368 | +0.039 | −0.013 |
| *Change detection mean* | | 53.1 | 58.7 | **59.9** | +5.6 | +1.2 |
| DIOR-RSVG localization | mIoU | **0.663** | 0.612 | 0.638 | −0.051 | +0.026 |
| DOTA localization | mIoU | 0.520 | 0.544 | **0.549** | +0.024 | +0.005 |
| FAIR1M localization | mIoU | **0.430** | 0.404 | 0.409 | −0.026 | +0.005 |
| *Object localization mean* | | **53.8** | 52.0 | 53.2 | −1.8 | +1.2 |
| *Mean of all 13 tasks* | | 70.80 | 75.39 | **75.40** | +4.59 | +0.02 |

top-left corner (55, 265), enlarged 5× (Fig. S3c). This region is on the left side of the image and does not contain the target. The final prediction, [88, 298, 118, 335], lies inside the second crop and has no overlap with the target (IoU 0.00). The standard API prediction, [90, 297, 120, 335], also has IoU 0.00. Thus, the additional crops did not correct the localization error in this example: the final box lies outside the target-containing first crop and inside the subsequent, target-free crop.

## S.8. PER-TASK RESULTS ACROSS REASONING-EFFORT SETTINGS

This section reports the results of the separate reasoning-effort experiment, in which the available effort levels are explicitly varied rather than using each model's default setting. Table S3 breaks down the average scores of GPT-6.1 Sol and Gemini 3.8 Flash in Fig. 6 of the main paper into all 13 tasks. For each model and task, all effort settings are scored on




Fig. S2. Autonomous Agents API trace for xView2 pre-disaster building counting, arranged by the four steps in Section S.5. (a) Enlarge: regions that the agent cropped from the pre-disaster image with ImageMagick, labeled with their enlargement factors; the dashed box is a second, 3× crop of the densest coastal block. (b) Inspect region by region: the four enlarged crops as the agent viewed them. (c) Record local counts: building centers that the agent wrote into its tally script, shown in the 3× re-check crop and colored by tally group (top, middle, bottom-left, bottom-right; same colors as the crops). Three entries are labeled as written in the script, as ($x$, $y$, damage level) in original-image pixels. (d) Aggregate with code: per-group counts summed by the script, compared with the standard API answer for the same image and the ground truth; the map on the right shows all recorded centers over the whole image. White boxes are the 189 ground-truth buildings, shown for reference only; they were not available to the agent.

the same test samples. From low to high effort, GPT-6.1 Sol improves on eight tasks, declines on four, and is unchanged on Landmarks recognition (0.885 at both settings).

## S.9. Linear Extrapolation of Task-Category Trends

As an exploratory exercise, we linearly extrapolate the five category trends in Fig. 3 of the main paper to estimate when their scores might reach 90. The category score of a model is the mean of its task scores on a 0–100 scale. For each category, we fit a model-level ordinary least-squares regression to the individual models in Fig. 3,

$$s_i = \beta\, t_i + \alpha_{f(i)} + \varepsilon_i, \tag{1}$$

where $s_i$ is the category score of model $i$, $t_i$ is its release date in decimal years, and $\alpha_f$ is the intercept of model family $f \in \{\text{GPT}, \text{Gemini}, \text{Qwen}, \text{LLaVA}\}$. The families share the slope $\beta$, which measures the annual improvement after accounting for the level differences between families. We report the trend line of the average family, whose intercept $\bar{\alpha}$ is the mean of the four family intercepts, and the year at which it reaches 90, $(90-\bar{\alpha})/\beta$. The 95% intervals come from bootstrap replicates that resample models with replacement within each family and refit the regression. We flag dates more than about three years after the last release (late 2029), a horizon equal to the length of the observed release period, as less reliable. As robustness checks, we refit the regression to the models released from May 2024 onward and with each family omitted in turn, and we test family-specific slopes against the common slope with an $F$-test. As an auxiliary estimate, we also fit a line to the means of the five 8-month release bins in Fig. 3, placing each bin at the mean release date of its models.

Table S4 and Fig. S4 summarize the results. All five categories improve over time, with slope intervals above zero. Object classification improves fastest, by 16.9 points per year ($R^2 = 0.45$), and its trend line reaches 90 in 2026.8 (95% interval 2026.5–2027.4); models released from May 2026 onward already average 90.5. Scene understanding improves by 7.0 points per year ($R^2 = 0.78$) and reaches 90 in 2028.7 (2027.7–2032.0). Object counting improves by 9.9 points per year ($R^2 = 0.60$) and reaches 90 in 2029.1 (2028.2–2031.6). Change detection and object localization improve by 6.4 and 11.0 points per year ($R^2 = 0.64$ and 0.71), but from lower levels, and their trend lines reach 90 only in 2034.8 and 2031.2, beyond the horizon. Family-specific slopes do not significantly improve the fit in any category ($p \geq 0.06$). The robustness refits move the projected years by at most 0.5 years, except for scene understanding (2028.2–2030.1) and change




Fig. S3. Autonomous Agents API trace for DIOR-RSVG referring-expression localization (prompt: "The storage tank is much smaller than the chimney in the middle"). (a) Input image with the two regions cropped by the agent. (b) First crop, enlarged 3×; it contains the target storage tank. (c) Second crop, enlarged 5×; it excludes the target and contains the agent's final box (solid orange). The dashed pink box is the standard API answer. Both predictions have IoU 0.00 with the target. Crop views are reconstructed from the input image using the logged crop coordinates and enlargement factors; the ImageMagick arguments are shown below each crop. The white ground-truth box is added for reference and was not available to the agent.

TABLE S3

PER-TASK SCORES OF GPT-6.1 SOL AND GEMINI 3.8 FLASH AT EACH REASONING-EFFORT SETTING. ACC.: ACCURACY; $r^2$: SQUARED PEARSON CORRELATION BETWEEN PREDICTED AND GROUND-TRUTH COUNTS; MACRO $r^2$: MEAN OVER THE FOUR DAMAGE LEVELS; MIOU: MEAN INTERSECTION OVER UNION. HIGHER IS BETTER FOR ALL METRICS. THE OVERALL MEAN IS REPORTED ON A 0–100 SCALE, AS IN THE MAIN TEXT. THE BEST SETTING OF EACH MODEL IN EACH ROW IS IN BOLD.

| | | GPT-6.1 Sol | | | | | Gemini 3.8 Flash | | |
|---|---|---|---|---|---|---|---|---|---|
| Task | Metric | Low | Medium | High | xhigh | Max | Low | Medium | High |
| DIOR-RSVG object classification | Acc. | 0.921 | 0.930 | 0.937 | **0.952** | 0.948 | 0.967 | 0.968 | **0.969** |
| PatternNet scene recognition | Acc. | **0.902** | 0.829 | 0.836 | 0.785 | 0.792 | 0.901 | 0.908 | **0.914** |
| Landmarks recognition | Acc. | 0.885 | 0.836 | 0.885 | 0.869 | **0.902** | **0.934** | **0.934** | 0.918 |
| RarePlanes aircraft counting | $r^2$ | **0.853** | 0.823 | 0.784 | 0.720 | 0.811 | 0.971 | 0.971 | **0.974** |
| COWC car counting | $r^2$ | 0.799 | 0.853 | **0.862** | 0.825 | 0.854 | **0.960** | 0.820 | 0.959 |
| xView2 building counting | $r^2$ | 0.669 | 0.725 | 0.738 | **0.808** | 0.759 | 0.716 | 0.731 | **0.781** |
| NEON tree counting | $r^2$ | **0.591** | 0.513 | 0.387 | 0.475 | 0.124 | 0.597 | 0.727 | **0.731** |
| Aerial animal counting | $r^2$ | 0.361 | **0.384** | 0.332 | 0.331 | 0.257 | 0.506 | 0.486 | **0.585** |
| xView2 change detection | Macro $r^2$ | 0.401 | 0.458 | **0.604** | 0.542 | 0.418 | 0.545 | 0.568 | **0.578** |
| FPCD farm-pond change detection | Acc. | 0.237 | 0.263 | **0.342** | 0.289 | 0.316 | 0.697 | **0.737** | 0.711 |
| DIOR-RSVG localization | mIoU | 0.484 | 0.486 | 0.504 | 0.534 | **0.552** | **0.472** | 0.404 | 0.450 |
| DOTA localization | mIoU | 0.393 | 0.420 | 0.436 | **0.443** | 0.437 | 0.344 | **0.442** | 0.423 |
| FAIR1M localization | mIoU | 0.372 | **0.393** | **0.393** | 0.381 | 0.386 | 0.263 | **0.324** | 0.291 |
| *Mean of all 13 tasks* | | 60.5 | 60.9 | **61.9** | 61.2 | 58.1 | 68.3 | 69.4 | **71.4** |

detection (2033.7–2036.8), and the bin-mean fit gives the same ordering of the categories, with years within one year of the model-level estimates except for change detection (2032.7).

Scores are bounded at 100, and future progress may be sub-linear, super-linear, or plateau. A score of 90 on the average-family trend line requires the typical model of each family, including small open-source models, to reach this level, which is stricter than the best model doing so. The extrapolations describe historical trends and are not forecasts of future model capabilities.

## S.10. ROBUSTNESS OF THE OVERALL SCORE

The overall score in the main paper is the equally weighted mean of 13 task scores measured with accuracy, $r^2$, and mIoU, so that each benchmark task has the same influence on the overall score. This section examines whether the model ranking and the progress across model generations depend on this choice. Three analyses each change one factor of the overall score: the weighting of the tasks, the metric of the counting tasks, and the set of tasks. All variants are computed for the 48 models of Fig. 2 of the main paper, and the Agents API is compared with the standard API of GPT-6 Astra on the paired samples of Table S2. Table S5 summarizes the results. In every variant, the model ranking remains highly consistent with that of the main paper (Spearman correlation 0.96–1.00), at least four of the five highest-scoring models are retained, newer models outperform older ones in 71–78% of model pairs, the latest release bin attains the highest mean score, and

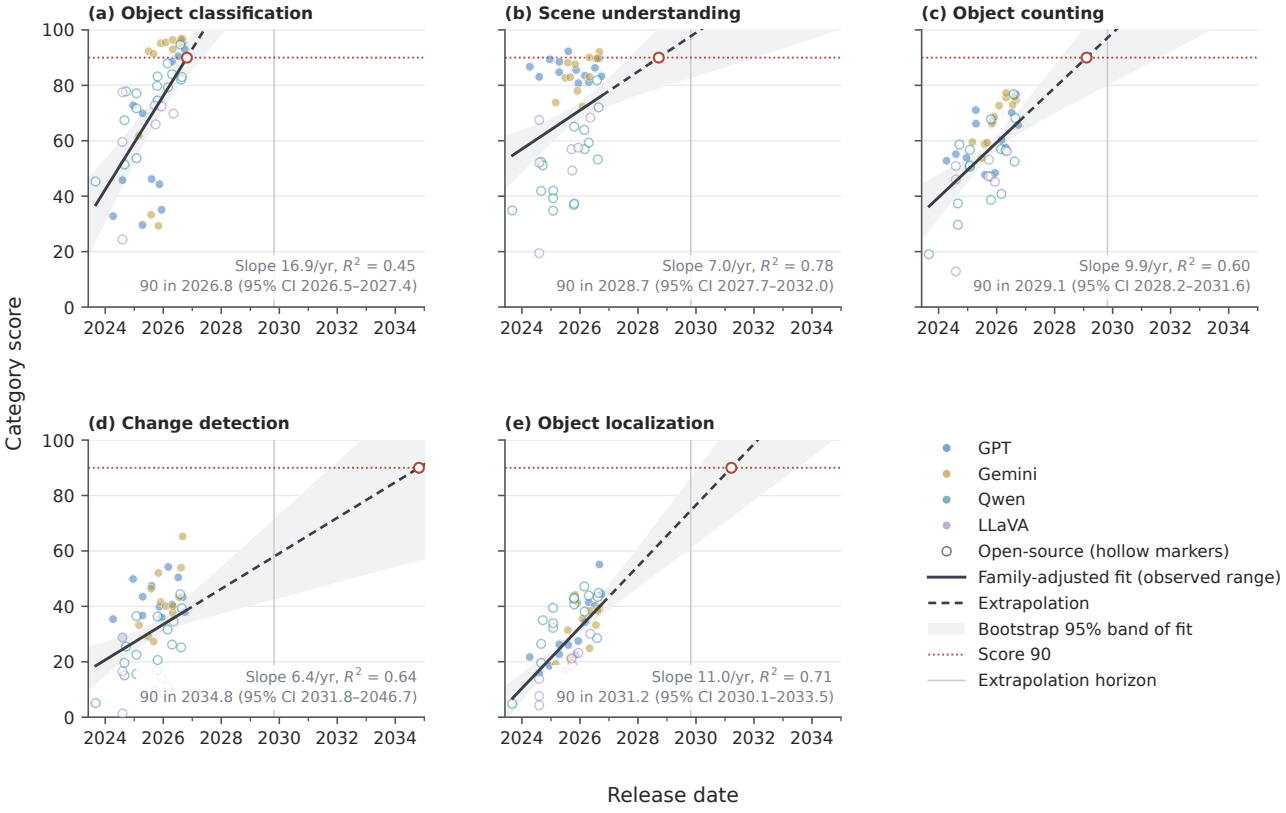



Fig. S4. Linear extrapolation of the five task-category trends in Fig. 3 of the main paper. Dots are individual models (filled: proprietary; hollow: open-source). The solid line is the average-family trend of the model-level regression with a common slope and family-specific intercepts over the observed period, and the dashed line is its extrapolation. Shading is the bootstrap 95% band of the trend line, the dotted line marks a score of 90, open circles mark where the trend line reaches 90, and the vertical line marks the extrapolation horizon (late 2029).

TABLE S4

MODEL-LEVEL LINEAR FITS WITH A COMMON SLOPE AND FAMILY-SPECIFIC INTERCEPTS FOR EACH TASK CATEGORY (0–100 SCALE). FITTED LATEST IS THE AVERAGE-FAMILY TREND VALUE AT THE LAST RELEASE (SEPTEMBER 2026). SLOPE IS IN POINTS PER YEAR, AND $R^2$ IS COMPUTED OVER MODELS. BRACKETS GIVE BOOTSTRAP 95% INTERVALS. SENSITIVITY GIVES THE RANGE OF THE YEAR ACROSS REFITS TO THE MODELS RELEASED FROM MAY 2024 ONWARD AND WITH EACH FAMILY OMITTED IN TURN. BIN MEAN GIVES THE YEAR FROM THE AUXILIARY FIT TO THE 8-MONTH BIN MEANS. ASSESSMENT GIVES THE CALENDAR YEAR IN WHICH THE TREND LINE REACHES 90; THE OTHER COLUMNS GIVE DECIMAL YEARS.

| Category | Fitted latest | Slope | $R^2$ | Year reaching 90 | Sensitivity | Bin mean | Assessment |
|---|---|---|---|---|---|---|---|
| Object classification | 88.8 | 16.9 [11.7, 22.0] | 0.45 | 2026.8 [2026.5, 2027.4] | 2026.7–2027.0 | 2026.7 | 2026 |
| Scene understanding | 76.2 | 7.0 [3.4, 10.9] | 0.78 | 2028.7 [2027.7, 2032.0] | 2028.2–2030.1 | 2028.2 | 2028 |
| Object counting | 66.7 | 9.9 [5.6, 13.6] | 0.60 | 2029.1 [2028.2, 2031.6] | 2028.7–2029.6 | 2028.3 | 2029 |
| Change detection | 38.2 | 6.4 [2.8, 9.5] | 0.64 | 2034.8 [2031.8, 2046.7] | 2033.7–2036.8 | 2032.7 | 2034 (beyond horizon) |
| Object localization | 40.6 | 11.0 [7.8, 13.8] | 0.71 | 2031.2 [2030.1, 2033.5] | 2031.0–2031.7 | 2031.4 | 2031 (beyond horizon) |

the Agents API improves the overall score of GPT-6 Astra.

### A. *Category-Balanced Weighting*

The category-balanced score gives each of the five task categories the same weight: it first averages the tasks within each of the five task categories and then weights each category by 20%. It preserves the model ranking (Spearman correlation 0.96) and the same five highest-scoring models, and the improvement across model generations becomes slightly steeper (12.3 instead of 11.3 points per year).

### B. *Alternative Counting Metrics*

The five counting tasks and xView2 change detection are scored with $r^2$ in the main paper. This analysis verifies the main conclusions with the mean absolute error (MAE) and the root mean squared error (RMSE) of the predicted counts. For a task with $n$ test images, ground-truth counts $y_i$ and predicted

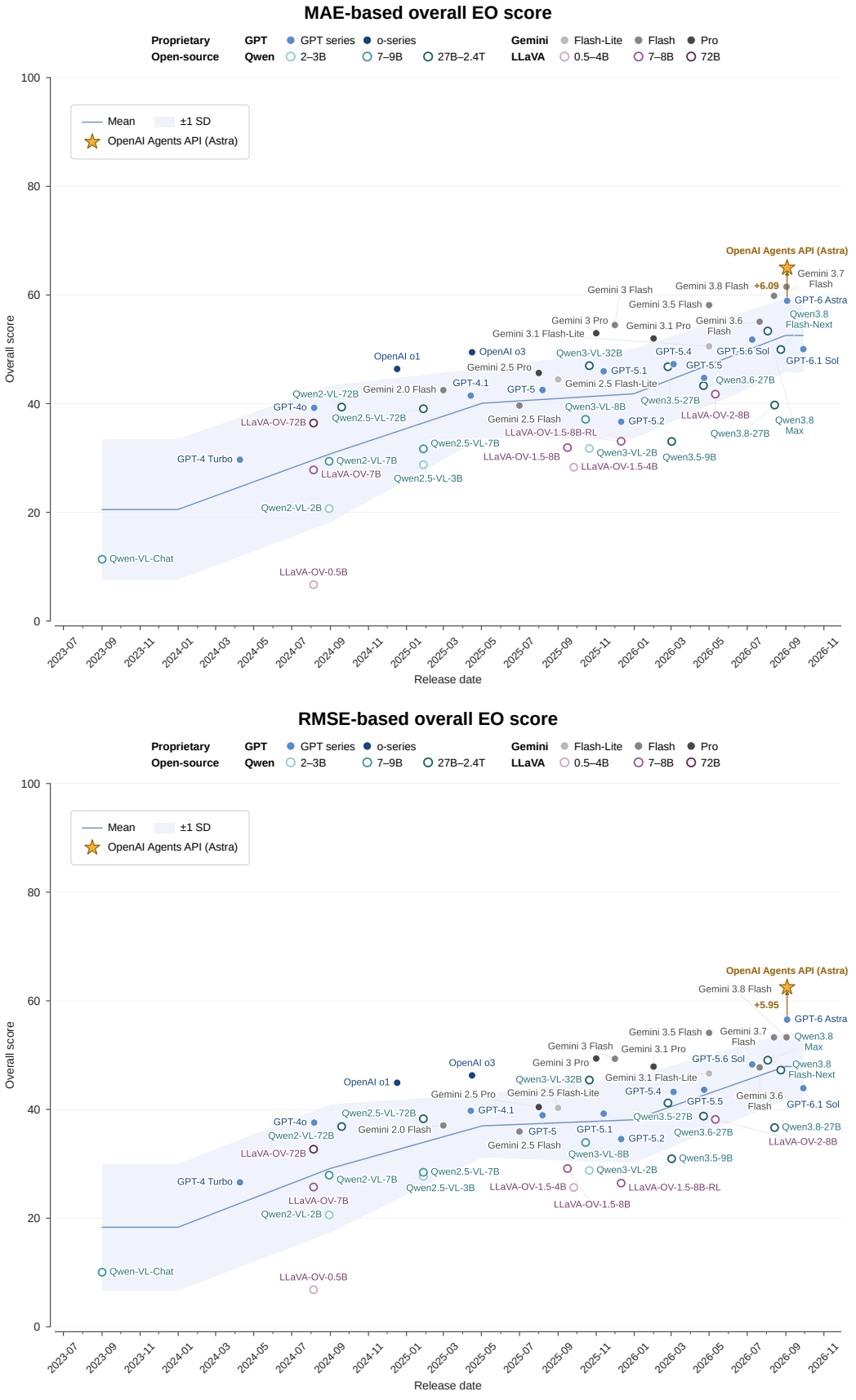



Fig. S5. MAE-based (top) and RMSE-based (bottom) versions of Fig. 2 of the main paper. The five counting tasks and xView2 change detection are scored with $s_{\mathrm{MAE}}$ or $s_{\mathrm{RMSE}}$; all other task scores are unchanged. The Astra point, agent star, and labeled gain use the same stratified random subset of up to 100 samples per task.

TABLE S5

ROBUSTNESS OF THE OVERALL SCORE IN FIG. 2 OF THE MAIN PAPER. EACH VARIANT CHANGES ONE FACTOR OF THE MAIN-PAPER SCORE (EQUALLY WEIGHTED TASKS, $r^2$ FOR THE COUNTING TASKS AND XVIEW2 CHANGE DETECTION). CATEGORY-EQUAL: EQUALLY WEIGHTED MEAN OF THE FIVE TASK CATEGORIES; MAE AND RMSE: THE SIX $r^2$ TASK SCORES REPLACED BY $s_{\mathrm{MAE}}$ OR $s_{\mathrm{RMSE}}$; LEAVE-ONE-TASK-OUT: RANGE OVER THE 13 SCORES THAT EACH OMIT ONE TASK. RANKING $\rho$: SPEARMAN CORRELATION WITH THE MODEL RANKING OF THE MAIN PAPER; TOP 5: MODELS SHARED WITH THE FIVE HIGHEST-SCORING MODELS OF THE MAIN PAPER; DATE $\rho$: SPEARMAN CORRELATION BETWEEN SCORE AND RELEASE DATE; SLOPE: LEAST-SQUARES TREND IN POINTS PER YEAR; BIN MEANS: FIRST AND LATEST 8-MONTH RELEASE BINS; NEWER: PERCENTAGE OF MODEL PAIRS IN WHICH THE MORE RECENTLY RELEASED MODEL SCORES HIGHER; AGENT GAIN: AUTONOMOUS AGENTS API MINUS STANDARD API FOR GPT-6 ASTRA ON THE PAIRED SAMPLES OF TABLE S2.

| Variant | Ranking $\rho$ | Top 5 | Date $\rho$ | Slope | Bin means | Newer (%) | Agent gain |
|---|---|---|---|---|---|---|---|
| Task-equal, $r^2$ (main paper) | 1.00 | 5 | 0.67 | 11.3 | 32.0 → 61.8 | 75 | 4.6 |
| Category-equal | 0.96 | 5 | 0.73 | 12.3 | 33.7 → 64.5 | 78 | 3.3 |
| MAE skill score | 0.97 | 4 | 0.72 | 11.2 | 20.5 → 52.4 | 77 | 6.1 |
| RMSE skill score | 0.96 | 4 | 0.67 | 9.8 | 18.3 → 47.6 | 75 | 6.0 |
| Leave-one-task-out | 0.98–1.00 | 4–5 | 0.59–0.69 | 10.6–12.0 | 27.6–34.6 → 59.2–64.2 | 71–76 | 2.4–5.4 |

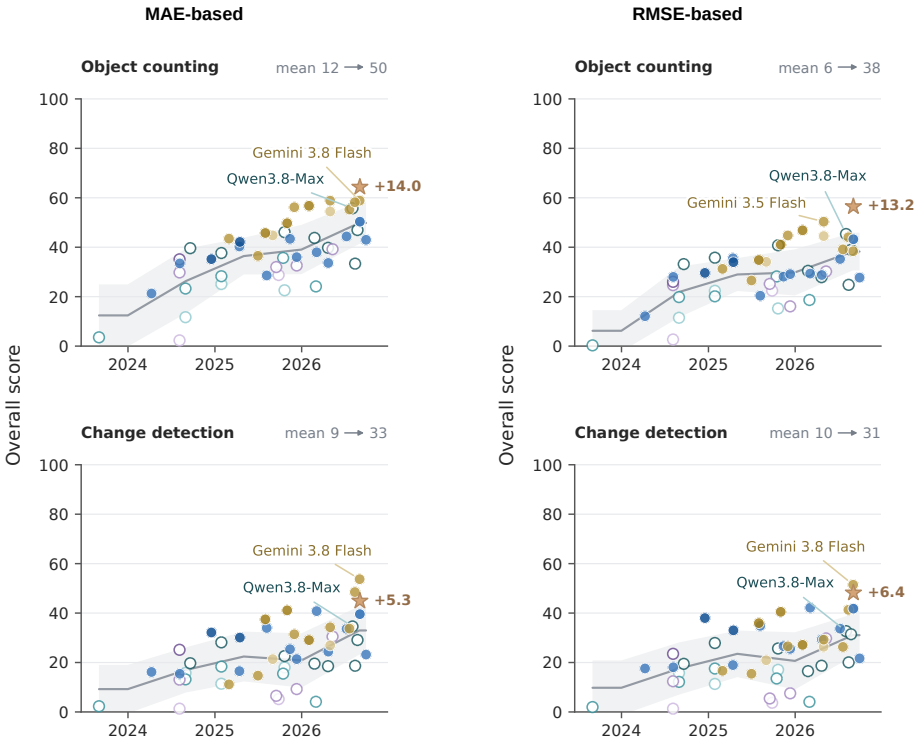



Fig. S6. MAE-based (left) and RMSE-based (right) versions of the object-counting (top) and change-detection (bottom) panels of Fig. 3 of the main paper. The Astra points, agent stars, and labeled gains use the same stratified random subset of up to 100 samples per task; the trend summaries use Astra's full-test scores.

counts $\hat{y}_i$,

$$\mathrm{MAE} = \frac{1}{n}\sum_{i=1}^{n}|\hat{y}_i - y_i|, \qquad \mathrm{RMSE} = \sqrt{\frac{1}{n}\sum_{i=1}^{n}(\hat{y}_i - y_i)^2}, \tag{2}$$

$$\%\mathrm{MAE} = 100 \times \frac{\sum_i |\hat{y}_i - y_i|}{\sum_i y_i}. \tag{3}$$

The errors are computed from the same predictions and parsing rules as $r^2$. For xView2 change detection, they are computed for each of the four damage levels and averaged, as for the macro-averaged $r^2$.

Because lower errors are better while the other task metrics are higher-is-better scores in $[0, 1]$, each error is converted into a skill score relative to the best constant prediction before it enters the overall and category scores:

$$s_{\mathrm{MAE}} = \max\left(0,\, 1 - \frac{\mathrm{MAE}}{\mathrm{MAE}_{\mathrm{ref}}}\right), \tag{4}$$

$$s_{\mathrm{RMSE}} = \max\left(0,\, 1 - \frac{\mathrm{RMSE}}{\mathrm{RMSE}_{\mathrm{ref}}}\right), \tag{5}$$

where $\mathrm{MAE}_{\mathrm{ref}}$ and $\mathrm{RMSE}_{\mathrm{ref}}$ are the errors obtained by predicting the median and the mean test-set count, respectively, for every image. A skill score of 1 denotes error-free counts and 0 denotes counts no better than the constant prediction; unlike $r^2$, the skill scores decrease when counts are systematically over- or underestimated. The skill scores place the error metrics on the same higher-is-better $[0, 1]$ scale as the other

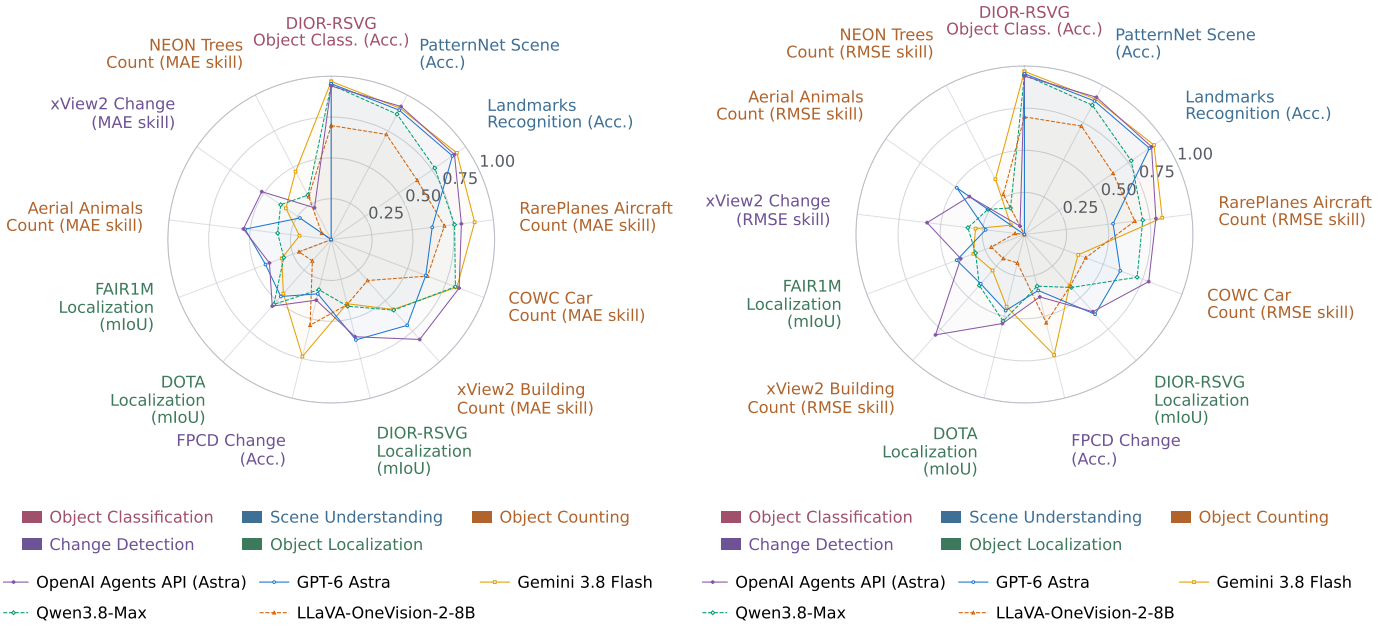



Fig. S7. MAE-based (left) and RMSE-based (right) versions of Fig. 4 of the main paper. Counting and xView2 change-detection axes show $s_{\mathrm{MAE}}$ and $s_{\mathrm{RMSE}}$; all other axes are unchanged.

TABLE S6
COUNTING ERRORS OF GPT-6 ASTRA UNDER THE STANDARD API (STD.), THE AUTONOMOUS AGENTS API (AUTO.), AND THE HUMAN-GUIDED AGENTS API (GUIDED) ON THE PAIRED SAMPLES OF TABLE S2 ($n = 100$ PER TASK). $\Delta$: AUTO.$-$STD. MAE WITH ITS PAIRED BOOTSTRAP 95% INTERVAL. FOR XVIEW2 CHANGE DETECTION, MAE AND RMSE ARE AVERAGED OVER THE FOUR DAMAGE LEVELS. LOWER IS BETTER.

| | MAE | | | | RMSE | | | %MAE | | |
|---|---|---|---|---|---|---|---|---|---|---|
| Task | Std. | Auto. | Guided | $\Delta$ [95% CI] | Std. | Auto. | Guided | Std. | Auto. | Guided |
| RarePlanes aircraft counting | 0.75 | 0.31 | 0.32 | $-0.44$ [$-0.94$, $-0.13$] | 2.38 | 0.66 | 0.72 | 29.2 | 12.1 | 12.5 |
| COWC car counting | 2.63 | 1.42 | 1.40 | $-1.21$ [$-1.79$, $-0.72$] | 4.78 | 3.30 | 3.04 | 23.1 | 12.5 | 12.3 |
| xView2 building counting | 11.05 | 10.41 | 8.99 | $-0.64$ [$-3.43$, 1.73] | 23.06 | 22.25 | 18.50 | 18.3 | 17.2 | 14.8 |
| NEON tree counting | 30.49 | 19.55 | 30.85 | $-10.94$ [$-15.33$, $-6.86$] | 51.08 | 32.54 | 52.85 | 92.2 | 59.1 | 93.3 |
| Aerial animal counting | 2.39 | 2.15 | 1.67 | $-0.24$ [$-0.73$, 0.30] | 3.64 | 4.02 | 3.53 | 32.0 | 28.8 | 22.4 |
| xView2 change detection | 4.91 | 4.25 | 4.10 | $-0.65$ [$-2.26$, 0.77] | 14.21 | 10.90 | 9.59 | – | – | – |

task scores; each task metric retains its own interpretation. In the MAE- and RMSE-based versions below, the six $r^2$ task scores are replaced by $s_{\mathrm{MAE}}$ or $s_{\mathrm{RMSE}}$, and all other task scores, models, and aggregation rules are those of the main paper.

### 1) Progress Across Model Generations

Fig. S5 shows the MAE- and RMSE-based versions of Fig. 2 of the main paper. The upward shift across model generations is preserved: the overall score increases by 11.2 (MAE) and 9.8 (RMSE) points per year, compared with 11.3 points per year with $r^2$, and the mean of the 8-month release bins rises from 20.5 to 52.4 (MAE) and from 18.3 to 47.6 (RMSE). The model ranking remains consistent with that of the main paper (Spearman correlation 0.97 and 0.96), and four of the five highest-scoring models are retained (Table S5).

Fig. S6 shows the corresponding object-counting and change-detection panels of Fig. 3. Newer models produce substantially smaller counting errors: the mean counting score rises from 12 to 50 (MAE) and from 6 to 38 (RMSE), and the mean change-detection score rises from 9 to 33 (MAE) and from 10 to 31 (RMSE). The other three panels of Fig. 3 do not involve counts and are unchanged.

### 2) Current Capability Boundaries

Fig. S7 shows the MAE- and RMSE-based versions of Fig. 4. Coarse-grained recognition remains the strongest capability, and counting performance again depends strongly on the target and background structure: aircraft and car counting reach the highest skill scores, whereas tree and animal counting have the lowest. The Agents API improves GPT-6 Astra on all six error-scored axes with MAE and on five of the six with RMSE.

### 3) Agent-Based Workflows

Table S6 reports the counting errors of GPT-6 Astra under the three workflows on the paired samples of Table S2. The autonomous Agents API lowers the MAE on all five counting tasks, and the paired bootstrap interval of the reduction excludes zero for aircraft (0.75 to 0.31), car (2.63 to 1.42),

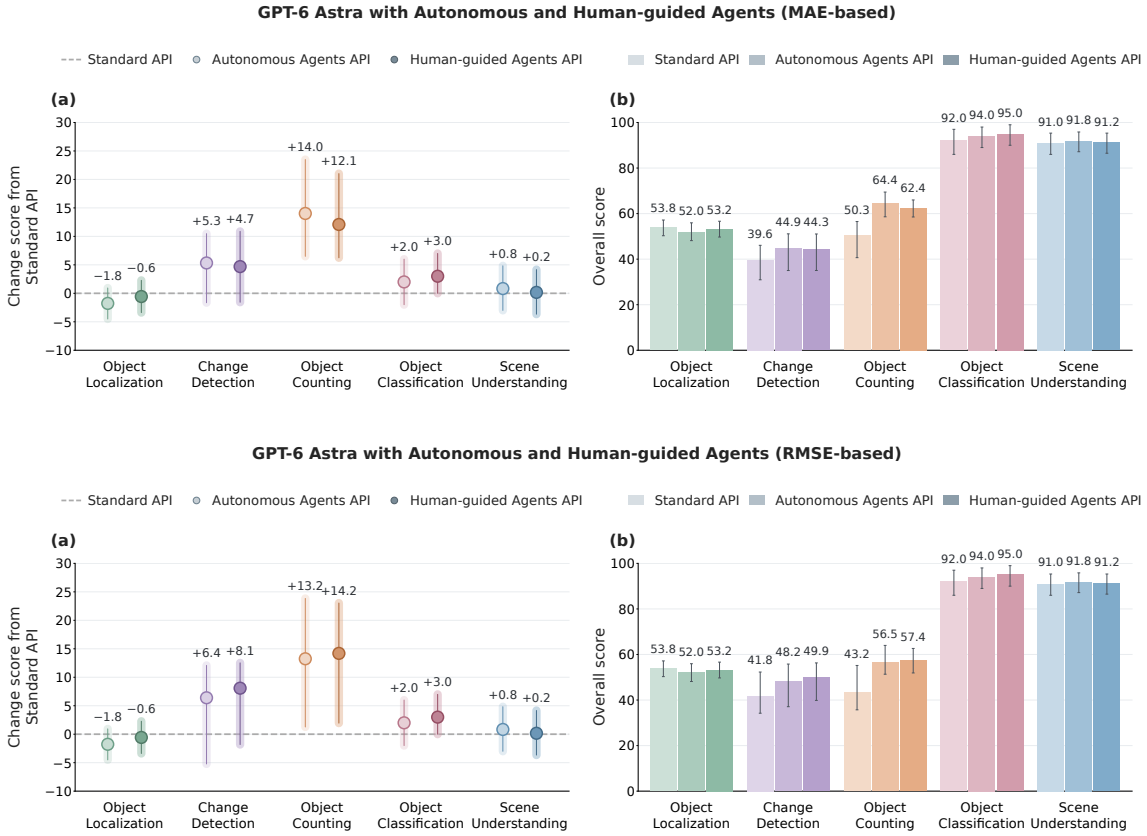



Fig. S8. MAE-based (top) and RMSE-based (bottom) versions of Fig. 8 of the main paper. The five counting tasks and xView2 change detection are scored with $s_{\mathrm{MAE}}$ or $s_{\mathrm{RMSE}}$; all other task scores are unchanged. Error bars denote 95% bootstrap confidence intervals.

TABLE S7

PERFORMANCE COMPARISON BETWEEN GPT-6 ASTRA AND SPECIALIZED EO MODELS ACROSS ALL 13 TASKS, WITH 95% BOOTSTRAP CONFIDENCE INTERVALS IN BRACKETS. ASTRA AND THE SPECIALIZED EO MODELS ARE EVALUATED ON IDENTICAL SAMPLES, USING HELD-OUT SUBSETS WHERE NEEDED TO AVOID OVERLAP WITH SPECIALIZED-MODEL TRAINING DATA. ASTRA'S SCORES THEREFORE DIFFER FROM THOSE ON THE FULL TEST SET. THE BETTER SCORE OF EACH PAIR IS IN BOLD.

| Task | Specialized EO model | Metric | GPT-6 Astra | Specialized |
|---|---|---|---|---|
| *Semantic recognition* | | | | |
| DIOR-RSVG Object Classification | Falcon, 2025 | Accuracy ↑ | 0.954 [0.941, 0.967] | **0.990** [0.983, 0.996] |
| PatternNet Scene Recognition | AiTLAS ResNet50, 2023 | Accuracy ↑ | 0.882 [0.836, 0.923] | **0.995** [0.985, 1.000] |
| Landmarks Recognition | MMCLIP, 2026 | Accuracy ↑ | **0.902** [0.820, 0.967] | 0.607 [0.475, 0.738] |
| *Counting* | | | | |
| RarePlanes Aircraft Counting | PromptAdaptOVD, 2025 | $r^2$ ↑ | 0.857 [0.770, 0.919] | **0.862** [0.794, 0.910] |
| | | MAE ↓ | 0.59 [0.51, 0.68] | **0.54** [0.47, 0.62] |
| COWC Car Counting | YOLOv3, 2022 | $r^2$ ↑ | 0.907 [0.863, 0.944] | **0.973** [0.954, 0.986] |
| | | MAE ↓ | 3.17 [2.84, 3.55] | **1.32** [1.16, 1.49] |
| xView2 Pre-disaster Building Counting | U-BDD++, 2023 | $r^2$ ↑ | **0.811** [0.731, 0.903] | 0.356 [0.264, 0.478] |
| | | MAE ↓ | **16.47** [12.56, 21.25] | 31.62 [26.33, 37.44] |
| NEON Tree Counting | DINO-Swin-L, 2026 | $r^2$ ↑ | 0.503 [0.374, 0.646] | **0.927** [0.884, 0.958] |
| | | MAE ↓ | 26.25 [21.04, 31.95] | **11.94** [9.87, 14.17] |
| Aerial Animal Counting | YOLOv8x, 2025 | $r^2$ ↑ | **0.755** [0.636, 0.846] | 0.569 [0.378, 0.732] |
| | | MAE ↓ | **2.27** [1.79, 2.78] | 3.32 [2.65, 4.08] |
| *Change detection* | | | | |
| xView2 Change Detection | DisasterAdaptiveNet, 2025 | Macro $r^2$ ↑ | 0.524 [0.460, 0.638] | **0.527** [0.480, 0.602] |
| | | MAE ↓ | **6.93** [5.63, 8.43] | 8.40 [6.98, 9.96] |
| FPCD Farm Pond Change Detection | EarthDial, 2025 | Accuracy ↑ | 0.342 [0.237, 0.447] | **0.382** [0.276, 0.487] |
| *Localization* | | | | |
| DIOR-RSVG Localization | GeoGround, 2024 | mIoU ↑ | 0.642 [0.597, 0.684] | **0.751** [0.717, 0.783] |
| DOTA Localization | GeoChat, 2024 | mIoU ↑ | **0.557** [0.443, 0.661] | 0.381 [0.277, 0.493] |
| FAIR1M Localization | EarthDial, 2025 | mIoU ↑ | **0.406** [0.334, 0.478] | 0.242 [0.181, 0.307] |

and tree counting (30.49 to 19.55), confirming that the agent workflow reduces actual counting errors. Fig. S8 shows the MAE- and RMSE-based versions of Fig. 8 of the main paper. With error-based scoring, the object-counting gain of the autonomous agent over the standard API is 14.0 (MAE) and 13.2 (RMSE) points, compared with 10.0 points with $r^2$.

### C. *Leave-One-Task-Out Analysis*

To test whether any single task dominates the overall score, each of the 13 tasks is omitted in turn and the overall score is recomputed from the remaining 12 tasks. The model ranking changes little (Spearman correlation 0.98–1.00), four or five of the five highest-scoring models are retained, and the fitted improvement ranges from 10.6 to 12.0 points per year. Omitting DIOR-RSVG object classification changes the ranking most (Spearman correlation 0.98), and omitting COWC car counting reduces the rise between the first and the latest release bin most (from 29.7 to 26.8 points). Omitting RarePlanes aircraft counting leaves the ranking nearly unchanged (Spearman correlation 0.99), and the agent gain remains positive in all 13 omissions (2.4 to 5.4 points).

## S.11. Confidence Intervals of the Overall Scores

Fig. S9 shows the overall EO score of each of the 48 models in Fig. 2 of the main paper with its 95% bootstrap confidence interval. For each model, test samples are resampled with replacement within each task; each draw recomputes every task metric with its original definition (accuracy, mIoU, or $r^2$ on the resampled set) and then the equally weighted overall score. The interval is given by the 2.5th and 97.5th percentiles of the draws. The half-widths of the overall-score intervals range from 1.5 to 6.1 points (median 2.9). For the five task-category scores, the median half-widths are 2.7 (object classification), 5.0 (scene understanding), 6.1 (object counting), 6.4 (change detection), and 1.5 (object localization) points.

## S.12. Full Comparison With Specialized EO Models

Table S7 extends Table I of the main paper with 95% bootstrap confidence intervals and the MAE of each counting task and xView2 change detection. For xView2 change detection, MAE is averaged over the four damage categories on the same 932 paired samples used for macro $r^2$; bootstrap resampling is performed at the image level. References for the tasks and specialized models are given in Table I of the main paper.

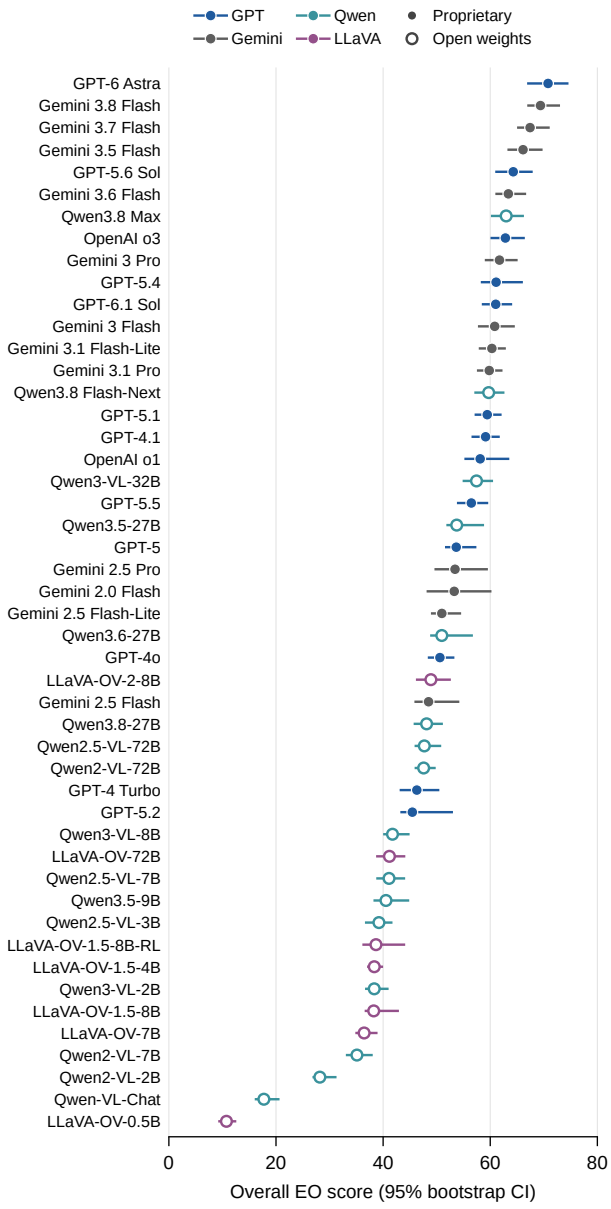



Fig. S9. Overall EO score of each model in Fig. 2 of the main paper with its 95% bootstrap confidence interval (test samples resampled within each task).